# Crystal plasticity modeling of strain-induced martensitic transformations to predict strain rate and temperature sensitive behavior of 304L steels: Applications to tension, compression, torsion, and impact

Zhangxi Feng<sup>a</sup>, Reeju Pokharel<sup>b</sup>, Sven C. Vogel<sup>b</sup>, Ricardo A. Lebensohn<sup>c</sup>, Darren Pagan<sup>d</sup>, Eloisa Zepeda-Alarcon<sup>b,e</sup>, Bjørn Clausen<sup>b</sup>, Ramon Martinez<sup>b</sup>, George T. Gray III<sup>b</sup>, Marko Knezevic<sup>a,\*</sup>

<sup>a</sup>Department of Mechanical Engineering, University of New Hampshire, Durham, NH 03824, USA.

<sup>b</sup>Materials Science and Technology Division, Los Alamos National Laboratory, Los Alamos, NM 87545, USA.

<sup>c</sup>Theoretical Division, Los Alamos National Laboratory, Los Alamos, NM, 87544, USA.

<sup>d</sup>Department of Materials Science and Engineering, Pennsylvania State University, University

Park, PA 16802, U.S.A

<sup>e</sup>Mission Support and Test Services, LLC

#### **Abstract**

This paper advances crystallographically-based Olson-Cohen (direct  $\gamma \to \alpha$ ') and deformation mechanism (indirect  $\gamma \rightarrow \varepsilon \rightarrow \alpha$ ') phase transformation models for predicting strain-induced austenite to martensite transformation. The advanced transformation models enable predictions of not only strain-path sensitive, but also of strain-rate and temperature sensitive deformation of polycrystalline stainless steels (SSs). The deformation of constituent grains in SSs is modeled as a combination of anisotropic elasticity, crystallographic slip, and phase transformation, while the hardening is based on the evolution of dislocation density and explicit shifts in phase fractions. Such grain-scale deformation is implemented within the meso-scale elasto-plastic self-consistent (EPSC) homogenization model, which is coupled with the implicit finite element (FE) method to provide a constitutive response at each FE integration point for solving boundary value problems at the macro-scale. Parameters pertaining to the hardening and transformation models within FE-EPSC are calibrated and validated on a suite of data including flow curves and phase fractions for monotonic compression, tension, and torsion as a function of strain-rate and temperature for wrought and additively manufactured (AM) SS304L. To illustrate the potential and accuracy of the integrated multi-level FE-EPSC simulation framework, geometry, mechanical response, phase fractions, and texture evolution are simulated during gas-gun impact deformation of a cylinder and quasi-static tension of a notched specimen made of AM SS304L. Details of the simulation framework, comparison between experimental and simulation results, and insights from the results are presented and discussed.

*Keywords*: Phase transformations; Microstructures; Crystal plasticity; Additive manufacturing; 304L steels

<sup>\*</sup> Corresponding author at: University of New Hampshire, Department of Mechanical Engineering, 33 Academic Way, Kingsbury Hall, W119, Durham, New Hampshire 03824, United States. Tel.: 603 862 5179; fax: 603 862 1865. E-mail address: marko.knezevic@unh.edu (M. Knezevic).

#### 1. Introduction

Austenitic stainless steels, such as 304L, have a wide range of applications, including marine, energy, aerospace, and medical sectors due to their corrosion resistance, high ductility, high strength, and large strain hardening capacity. Components made of austenitic steels used in these industries undergo shaping operations and simulation tools are vital in the optimization of these shaping operations as well as the evaluations of component performance in service (Ardeljan et al., 2014; Hosford and Caddell, 1993; Knezevic et al., 2016). In such simulations, a constitutive law represents the material behavior under an applied deformation. Constitutive laws are needed as part of the solution of the fundamental balance of linear momentum governing equation of continuum mechanics. The solution over a given geometry in terms of a pair of work-conjugated stress and strain measures is usually sought numerically using the finite elements method (FEM) (Ardeljan et al., 2015; Bathe, 1996; Eghtesad et al., 2018a; Eghtesad et al., 2022). Accuracy of simulations is influenced by accuracy of the constitutive law.

A good combination of strength and ductility exhibited by austenitic stainless steels is provided by the transformation-induced plasticity (TRIP) phenomenon. The TRIP phenomenon of transforming the metastable austenite into thermodynamically stable hard martensite delays local damage and permits greater uniform elongation prior to necking, resulting in high ductility and strength. To promote high ductility along with moderate hardening, the transformation rate should be slow enough so that the TRIP completes at larger strains (Bhowmik et al., 2022b; Spencer et al., 2009). In contrast, high rates of austenite into martensite transformation result in rapid saturation of martensite content and completion of the TRIP at small strains providing rapid hardening but small ductility. Therefore, the kinetics of transformation during deformation influences the overall deformation behavior of the austenitic steels.

In strain-induced TRIP, the face-centered cubic (FCC) γ-austenite phase transforms into an intermediate hexagonal close-packed (HCP)  $\varepsilon$ -martensite phase, which then transforms into a body-centered tetragonal (BCT)  $\alpha'$ -martensite phase (approximated as the body-centered cubic (BCC) structure) (Olson and Cohen, 1972, 1975; Talonen and Hänninen, 2007). α-martensite nucleates at the intersection of shear bands formed during plastic deformation of austenite. The bands form by separation of perfect dislocations into Shockley partial dislocations characterized by the stacking fault width (SFW) (Olson and Cohen, 1976; Talonen and Hänninen, 2007). The bands are either ε-martensite or twins, determined by their stacking fault energy (SFE) of the steel, which is primarily dependent on chemical composition. Additionally, the transformation process is highly dependent on crystal orientations and grain size, in addition to temperature, strain state/level, and strain-rate (Burgers and Klostermann, 1965; Goodchild et al., 1970; Lagneborgi, 1964; Petit et al., 2007; Polatidis et al., 2020; Zecevic et al., 2019). Transformation proceeds with increasing plastic strain through the growth of already nucleated martensite along with formation of additional nucleation sites and their subsequent coalescence after impingement of the closely spaced nucleated martensite until a saturated fraction of martensite is reached. Some pockets of untransformed austenite are unavoidable because the intersection of the shear bands becomes less probable as the transformation nears completion (Murr et al., 1982).

Several phenomenological kinetic models have been developed to predict fraction of martensite with plastic strain (Ahmedabadi et al., 2016; Angel, 1954; Eghtesad et al., 2022; Ludwigson and Berger, 1969; Matsumura et al., 1987; Olson and Cohen, 1972, 1975; Shin et al., 2001). These models typically assume a sigmoidal shape for the  $\alpha'$ -martensite volume fraction evolution with respect to strain (Olson and Cohen, 1975; Santacreu et al., 2006). One of the major limitations of

these models is their inability to predict saturated fraction of martensite. A number of studies have extended the phenomenological formulations to introduce strain-path sensitivity through the consideration of stress triaxiality and Lode angle parameter on the transformation kinetics (Ardeljan et al., 2016b; Beese and Mohr, 2011; Haidemenopoulos et al., 2014; Kim et al., 2015; Lebedev and Kosarchuk, 2000; Mansourinejad and Ketabchi, 2017; Santacreu et al., 2006; Stringfellow et al., 1992). Nevertheless, the phenomenological models are not able to represent the SFW and shear bands dependence on the loading. To overcome these limitations, the Olson-Cohen (OC) model was implemented in homogenization-based crystal plasticity models like a visco-plastic self-consistent (VPSC) model (Wang et al., 2016). Although the effect of crystallographic texture evolution and anisotropy on the transformation kinetics was considered by (Wang et al., 2016), their model assumed that the evolution of volume fraction of  $\alpha'$ -martensite only depends on plastic strain and not on strain-path. As a result, two different grains with the same strain profile would have identical transformation behavior.

Recognizing the above limitation of the transformation model implementation in VPSC, another crystallographic extension of the OC model was implemented in an elasto-plastic self-consistent (EPSC) crystal plasticity model (Zecevic et al., 2019). In addition to the crystallography of the transformation mechanisms, in this model the transformation propensity at the grain level was sensitive to stress through two mechanisms: (1) the resolved shear stress on a slip plane in the direction normal to the Burgers vector controls the stacking fault width (SFW), which in turn controls the potential nucleation sites, and (2) the stress triaxiality controls the probability of the  $\alpha$ '-martensite formation at a nucleation site. In the present work, this phase transformation (PT) model in EPSC will be referred to as OCPT. More recently, a deformation mechanism (DM)-based phase transformation model for strain-induced phase transformation was proposed and implemented in EPSC (Feng et al., 2021). Here, this PT model will be referred to as DMPT. The DMPT model circumvents the sigmoidal function for the evolution of  $\alpha$ '-martensite intrinsic to the OCPT model by modeling the nucleation and growth of  $\varepsilon$ -martensite grains explicitly as shear bands resulting from separation of partial dislocations. Moreover, the nucleation and growth of  $\alpha$ '-martensite grains are consequences of shear bands intersections.

The objective of the present work is to incorporate strain-rate and temperature sensitivity into the OCPT and DMPT models and to demonstrate their flexibility and utility through several case studies. Plasticity and underlying strain-induced martensitic transformation in wrought and additively manufactured (AM) 304L steels are predicted during tension, compression, torsion, and gas-gun (Taylor impact) deformation using the aforementioned models within a EPSC-based finite element (FE) implementation (FE-EPSC). Parameters of the hardening and transformation models within FE-EPSC are calibrated and validated on a suite of data including flow curves and phase fractions for monotonic compression, tension and torsion as a function of strain-rate and temperature for wrought and AM SS304L. Subsequently, the model is applied to simulate a gas gun impact deformation of a cylinder and a quasi-static tension of a notched specimen made of AM SSs. While the dynamic case provided a broad range of strain level, strain-rate, and temperature conditions to evaluate the predictive capability of the model, the quasi-static case allowed variations of strain levels, stress state, and triaxiality. Geometrical features and microstructures in terms of spatial fields of phase fraction and texture evolution are measured and used to experimentally verify the models. It is shown that the appropriate modeling of phase fractions and crystallography facilitates predicting the experimentally measured data. Performances of the two models are compared and discussed in terms of predicted geometry,

strength, phase fractions, and texture evolution as a function of strain level, stress state, strain-rate, temperature, and initial microstructures in wrought and AM samples of 304L steels.

# 2. Modeling framework

#### 2.1 EPSC model

This section summarizes the crystal plasticity constitutive law used to perform the simulations in the present work. The law is an implicit formulation of the EPSC model (Zecevic and Knezevic, 2019) incorporating the phase transformation sub-models (Feng et al., 2021; Zecevic et al., 2019), and embedded in the implicit FEM framework (Barrett and Knezevic, 2019; Barrett et al., 2020; Zecevic et al., 2017). The embedded model is termed FE-EPSC. In what follows, dot and tensor products are indicated by • and  $\bigotimes$ , respectively.

EPSC relies on the Jaumann rate of Cauchy stress,  $\hat{\sigma}$ , and the strain-rate,  $\dot{\epsilon}$  (Ferreri et al., 2022; Ghorbanpour et al., 2020; Nagtegaal and Veldpaus, 1984; Neil et al., 2010; Zecevic et al., 2015)

$$\widehat{\mathbf{\sigma}} = \dot{\mathbf{\sigma}} + \mathbf{\sigma} \mathbf{W} - \mathbf{W} \mathbf{\sigma}. \tag{1}$$

The constitutive equation applies to a material point, whether the latter is a polycrystalline aggregate or a single crystal. The tensorial quantities in the equation,  $\sigma$  and  $\mathbf{W}$  are the Cauchy stress and spin respectively. The corresponding quantities at crystal-level are denoted with the superscript c as  $\sigma^c$  and  $\mathbf{W}^c$ . Furthermore, the crystal Jaumann rate of Cauchy stress and strainrate are  $\hat{\sigma}^c$  and  $\dot{\mathbf{E}}^c$ .

To incorporate the phase transformation mechanics, the crystal-level Jaumann rate constitutive relation is adjusted to incorporate the phase transformation strain-rate as (Zecevic et al., 2019)

$$\widehat{\mathbf{\sigma}}^c = \mathbf{C}^c (\dot{\mathbf{\varepsilon}}^c - \dot{\mathbf{\varepsilon}}^{pl,c} - \dot{\mathbf{\varepsilon}}^{pt,c}) - \mathbf{\sigma}^c tr(\dot{\mathbf{\varepsilon}}^c), \tag{2}$$

where  $\mathbf{C}^c$  is the 4<sup>th</sup> rank single crystal elastic stiffness tensor,  $\dot{\mathbf{E}}^{pt,c}$  is the phase transformation strain-rate,  $\dot{\mathbf{E}}^{pl,c}$  is the plastic strain-rate, and  $\dot{\mathbf{E}}^c$  is the total strain-rate. The plastic strain-rate is a sum of the products between the Schmid tensor,  $\mathbf{m}^s = \frac{1}{2}(\mathbf{b}^s \otimes \mathbf{n}^s + \mathbf{n}^s \otimes \mathbf{b}^s)$  and shear rates,  $\dot{\gamma}^s$ , over available slip systems, s, per grain, c, i.e.  $\dot{\mathbf{E}}^{pl,c} = \mathbf{m}^s \dot{\gamma}^s$ . The Schmid tensors are defined based on the slip directions parallel to the Burgers vectors,  $\mathbf{b}^s$ , and the slip system normals,  $\mathbf{n}^s$ .

The crystal and polycrystal constitutive relations can conveniently be expressed as

$$\widehat{\mathbf{\sigma}}^c = \mathbf{L}^c (\dot{\mathbf{\epsilon}}^c - \dot{\mathbf{\epsilon}}^{pt,c}),\tag{3a}$$

$$\widehat{\mathbf{\sigma}} = \mathbf{L}(\dot{\mathbf{\varepsilon}} - \dot{\mathbf{\varepsilon}}^{pt}),\tag{3b}$$

where **L**<sup>c</sup> and **L** are the elasto-plastic stiffness tensors at the crystal and polycrystal levels. The crystal stiffness is derived from Eq. (2) and using the hardening law for the evolution of slip resistance (Nugmanov et al., 2018; Turner and Tomé, 1994; Zecevic and Knezevic, 2018a). The polycrystal stiffness is evaluated using the basic SC homogenization procedure (Eshelby, 1957; Ghorbanpour et al., 2017; Lipinski and Berveiller, 1989; Neil et al., 2010; Risse et al., 2017; Turner and Tomé, 1994) starting from the volume averages

$$\widehat{\mathbf{\sigma}} = \langle \widehat{\mathbf{\sigma}}^c \rangle \text{ and } \dot{\mathbf{\varepsilon}} = \langle \dot{\mathbf{\varepsilon}}^c \rangle.$$
 (4)

Activation of slip systems is given by the following conditions

$$\mathbf{\sigma}^c \cdot \mathbf{m}^s = \tau_c^s, \tag{5a}$$

$$\widehat{\mathbf{\sigma}}^c \cdot \mathbf{m}^s = \dot{\tau}_c^s, \tag{5b}$$

where,  $\tau_c^s$  is a value of critical resolved shear stress value or slip resistance. The condition in Eq. (5a) ensures that the stress is on the yield surface, while the condition in Eq. (5b) is the consistency condition ensuring that the stress stays on the yield surface (Knockaert et al., 2000; Zecevic et al., 2019). The evolution law for slip resistance will be described later.

Crystal lattice reorientation with plastic strain is driven by spin tensors

$$\mathbf{W}^c = \mathbf{W}^{c,app} - \mathbf{W}^{pl,c},\tag{6}$$

where  $\mathbf{W}^{c,app}$  and  $\mathbf{W}^{pl,c}$  are applied spin and plastic spin tensors. The latter is calculated using  $\mathbf{W}^{pl,c} = \sum_{s} \dot{\gamma}^{s} \mathbf{q}^{s}$  with  $\mathbf{q}^{s} = \frac{1}{2} (\mathbf{b}^{s} \otimes \mathbf{n}^{s} - \mathbf{n}^{s} \otimes \mathbf{b}^{s})$ .

## 2.2 Modeling strain-induced martensitic transformation during plastic deformation

Strain-induced phase transformation begins by the formation of slip bands (Olson and Cohen, 1976). The bands occur as partial dislocations sufficiently separate to form a thick stacking fault, which eventually spans the whole grain under the action of local stress. The stacking fault width (SFW) i.e. the separation between partials is (Zecevic et al., 2019)

$$d = cN^2/(2\gamma_N - Nb_p\left(\left(\hat{\mathbf{b}}_l^s - \hat{\mathbf{b}}_r^s\right)\boldsymbol{\sigma}^c\right) \cdot \hat{\mathbf{n}}^s),\tag{7}$$

where N is the number of intrinsic SF in the slip band,  $b_p = \frac{a_p}{\sqrt{6}}$  is the Burgers vector magnitude of a partial dislocation,  $\gamma_N$  is the fault energy,  $\hat{\mathbf{b}}_l^s$  is a left partial unit vector,  $\hat{\mathbf{b}}_r^s$  is a right partial unit vector,  $\mathbf{\sigma}^c$  is a crystal stress,  $\hat{\mathbf{n}}^s$  is the slip plane normal vector, and c is a constant given in (Zecevic et al., 2019). As the denominator in Eq. (7) approaches zero under the stress,  $\mathbf{\sigma}^c$ , the separation, d, approaches infinity i.e., the whole grain. Therefore, an active slip system, s, forms a slip band if

$$\frac{2\gamma_N}{N} - b_p \left( \left( \hat{\mathbf{b}}_l^S - \hat{\mathbf{b}}_r^S \right) \mathbf{\sigma}^c \right) \cdot \hat{\mathbf{n}}^S = 0, \tag{8}$$

where,  $\gamma_N/N$  is the stacking fault energy (SFE), which is a material constant.

The band is comprised of  $\varepsilon$ -martensite, which has a hexagonal close-packed (HCP) structure. The  $\varepsilon$ -martensite structure results from T/2 shear carried out by shuffles on every  $2^{\rm nd}$  {111} $_{\gamma}$  plane for  $\frac{a_{\gamma}}{12}\langle 1\bar{1}\bar{2}\rangle_{\gamma}$ .  $T=\frac{b_p}{d_{111}}=\frac{1}{\sqrt{2}}$  is the twinning shear, where  $d_{111}$  is the spacing between the {111} $_{\gamma}$  planes. The formation of one slip band is assumed to trigger the creation of multiple slip bands on active slip systems. Partial dislocations gliding on other active slip systems can intersect a given slip band. The intersected region undergoes the transformation from  $\varepsilon$ -martensite to  $\alpha$ '-martensite. The transformation is a consequence of a T/3 shear introduced by the intersecting shear band. The T/3 shear is on  $\{01\bar{1}1\}_{\varepsilon}$  planes within the T/2 structure meaning that the glide in the given band operates on pyramidal slip systems (Yang et al., 2015). The intersection of the T/2 and T/3 shear bands has the BCC structure. The  $\alpha$ '-martensite is only the intersected region. After forming the intersecting region, which grows with shearing.

The process described above consisting of shear band formation driven by the local stress state,  $((\hat{\mathbf{b}}_l - \hat{\mathbf{b}}_r)\boldsymbol{\sigma}^c)\cdot\hat{\mathbf{n}}$ , is responsible for the stress sensitivity of the phase transformation models employed in the present work. Common to the models is the calculation of phase transformation strain. Since the shear part of the phase transformation strain is accommodated as slip and shear band formation processes, the actual phase transformation strain is only the volume change. Given the lattice parameters of austenite,  $a_{\gamma}$ =0.3589 nm, and martensite,  $a_{\alpha'}$ =0.2873 nm, (Wang et al., 2016), the increase in volume is 2.59%. Given the volumetric part of the Bain deformation gradient (Bhadeshia, 2001; Cahn et al., 1996),  $\mathbf{F}^{vol}$ , the strain is

$$\mathbf{\varepsilon}^{pt} = \frac{\left(\mathbf{F}^{vol}\right)^T \mathbf{F}^{vol} - \mathbf{I}}{2}.\tag{9}$$

Finally, common to both models is the determination of crystal lattice orientation of nucleating  $\varepsilon$ -martensite and then  $\alpha'$ -martensite. The crystal re-orientation relationships from parent  $\gamma$ -austenite grain to  $\varepsilon$ -martensite grain to  $\alpha'$ -martensite grain are (Bogers and Burgers, 1964; Bracke et al., 2007)

$$\{111\}_{\gamma} \parallel \{0001\}_{\varepsilon} \parallel \{110\}_{\alpha'} \tag{10a}$$

$$\langle 110 \rangle_{\nu} \parallel \langle 2\overline{1}\overline{1}0 \rangle_{\varepsilon} \parallel \langle 111 \rangle_{\alpha'} \tag{10b}$$

The model identifies two slip systems carrying out T/2 and T/3 shears for  $\varepsilon$ -martensite grain and  $\alpha'$ -martensite grain formation. While bands of  $\varepsilon$ -martensite corresponding to all active slip systems per grain are created with their respective crystal orientations and volume fractions and added to the polycrystalline aggregate, only one band with the greatest separation (Eq. 7) is selected to re-orient into an  $\alpha'$ -martensite grain. Therefore, in our simplified implementation one  $\gamma$ -austenite grain is producing one  $\alpha'$ -martensite grain. The initial field variables in newly created  $\varepsilon$ -martensite grains are set equal to those in the parent  $\gamma$ -austenite grain. The highest resolved shear stress plane and direction for the T/3 shear within  $\varepsilon$  gives rise to the  $\alpha'$ -martensite grain crystal lattice orientation respecting Eq. (10), which is added to the polycrystalline aggregate. State variables from  $\varepsilon$  are transferred to  $\alpha'$ . The difference between the OCPT and DMPT models pertaining to the crystal lattice reorientation is that the former model does not nucleate the  $\varepsilon$ -phase.

## 2.2.1 Olson-Cohen phase transformation (OCPT) model

The original OCPT model (Olson and Cohen, 1975) empirically relates the macroscopic volume fraction of the  $\alpha'$  martensite phase,  $f^{\alpha'}$ , to the macroscopic strain,  $\varepsilon$ 

$$f^{\alpha'} = 1 - \exp\{-\beta [1 - \exp(-\alpha \varepsilon)]^n\}$$
(11)

The parameters  $\alpha$  and  $\beta$  represent phenomenologically the rate of shear-band formation and the nucleation probability of a martensite grain at an intersection of shear bands, respectively. The parameter n informs the model of the number of shear band intersections given existence of the shear bands. Although these parameters give some physical interpretation of the involved phenomena, they are fitted to the experimentally measured data of volume fraction evolution. Therefore, the fitting parameters are averaged characteristics influenced by material properties and loading conditions such as temperature and strain-rate.

In a recent work (Zecevic et al., 2019), a crystallographic extension to the empirical OCPT model has been developed and successfully applied to predicting strain path dependence of martensitic transformation. The extension accounts for the stress state at the grain level and the crystallography of the transformation mechanism. Based on Eq. (8), the stress state influences the potential nucleation site. Moreover, the stress triaxiality influences the probability of the  $\alpha'$ -martensite formation at a nucleation site. The extended model was implemented in EPSC and used to predict the stress state and texture dependence of the strain-induced  $\alpha'$ -martensite transformation and mechanical response of austenitic steels.

The extended OCPT model considers the  $\alpha$  and  $\beta$  parameters as functions of stress state and strain-rate at the crystal level

$$\alpha = \alpha_0 + K_\alpha \, x_\alpha(\mathbf{\sigma}^c) \tag{12a}$$

$$\beta = \beta_0 + K_\beta \, x_\beta(\mathbf{\sigma}^c) \tag{12b}$$

where  $\alpha_0$ ,  $K_\alpha$ ,  $\beta_0$ , and  $K_\beta$  are fitting parameters.  $x_\alpha(\mathbf{\sigma}^c)$  and  $x_\beta(\mathbf{\sigma}^c)$  draw information about the stress state of the crystal using

$$x_{\alpha} = \sum_{s} \frac{\left( (\hat{\mathbf{b}}_{l}^{s} - \hat{\mathbf{b}}_{r}^{s}) \sigma^{c} \right) \cdot \hat{\mathbf{n}}^{s}}{|\sigma^{c} \cdot \mathbf{m}^{s}| \, n_{act}}$$
 (13a)

$$x_{\beta} = -\frac{p}{\sigma^{eq}} \tag{13b}$$

where  $x_{\alpha}$  is derived from the mechanics of shear band formation (Eq. 8), which is a prerequisite for strain-induced transformation. The equation is conveniently normalized by the resolved shear stress and the number of active slip systems in a given grain,  $n_{act}$ . As the set of active slip systems in a single grain under a given stress state depends on the crystal orientation, the  $x_{\alpha}$  term incorporates the effect of crystallographic orientation into the rate of shear-band formation. To introduce strain-rate sensitivity, we implement a new power law equation to scale the transformation nucleation rate via the  $\beta_0$  term from Eq. (12b)

$$\beta_0 = \beta_{0,C} \dot{\varepsilon}^{\beta_{0,n}} \tag{14}$$

where  $\beta_{0,C}$  and  $\beta_{0,n}$  are fitting constants.  $\beta_{0,C}$  replaces the original  $\beta_0$  term, while  $\beta_{0,n}$  scales the macroscopic strain-rate,  $\dot{\varepsilon}$ . When the strain-rate is quasi-static, the equation yields the value for  $\beta_0$  typically used for quasi-static monotonic loading simulations.  $x_{\beta}$  is the ratio between hydrostatic pressure and von Mises stress, i.e. the stress triaxiality factor, influencing the martensite grain nucleation probability at an intersection of shear bands.

Once the transformation condition driven by local stress and SFE is satisfied (Eq. 8), the  $\alpha'$ -martensite phase transformation begins. The volume fraction evolution is governed by the incremental form of Eq. (11) at the crystal level

$$df^{\alpha'} = (1 - f^{\alpha'})\beta n(f^{sb})^{n-1}df^{sb},\tag{15a}$$

$$df^{sb} = \alpha(1 - f^{sb})d\varepsilon, \tag{15b}$$

where  $f^{sb}$  is the shear band volume fraction. The incremental form is used since  $\alpha$  and  $\beta$  are dependent on the evolving stress/strain states per grain. The volume fraction of transformed martensite grain is correspondingly

$$dw^{c,m} = (w_0^c - w^{c,m})\beta n(f^{c,sb})^{n-1}df^{c,sb}$$
(16a)

$$df^{c,sb} = \alpha (1 - f^{c,sb}) \sum_{s} d\gamma^{s}$$
(16b)

where  $w_0^c$  is the initial parent austenite grain volume fraction and  $\sum_s d\gamma^s$  is the sum of shearing strains on slip systems per grain. As the volume fraction of  $\alpha'$ -martensite in a parent austenite grain attains 1%, the new grain is created and added to the polycrystal. One  $\alpha'$ -martensite grain can nucleate per austenite grain, which is predominantly the case in experimental observations by EBSD (Das et al., 2016). The martensite volume fraction evolves as a function of shear strain in each austenite crystal. The crystal stress and state variables of the austenite parent grain are assigned to the new  $\alpha'$ -martensite grain. As initial volume fraction of  $\alpha'$ -martensite is very small, this initial assumption for the stress and state variables of martensite is not appreciably important for the predictions of the mechanical response. Martensite has higher slip resistance than austenite and, therefore, deforms elastically while increasing the stress with further straining. The initial value of slip resistance and the other hardening parameters for the evolution of slip resistance are fitting parameters, as will be described later. More details of the numerical implementation of the OCPT model within EPSC are provided in (Zecevic et al., 2016c).

#### 2.2.2 Deformation mechanisms phase transformation (DMPT) model

In the DMPT model, we distinguish the FCC  $\gamma$ -austenite to HCP  $\varepsilon$ -martensite transformation and then the HCP  $\varepsilon$ -martensite to BCC  $\alpha'$ -martensite transformation. The formulation for modeling of the two subsequent phases of transformations is described in detail in (Feng et al., 2021) and is briefly summarized here, starting with the  $\gamma$  to  $\varepsilon$  transformation.

The increment of  $\varepsilon$ -martensite volume fraction is

$$\Delta f^{s,\varepsilon} = \frac{\Delta \gamma^{s,p}}{s^{\varepsilon}} \tag{17}$$

where  $\Delta \gamma^{s,p}$  is the shearing strain increment in the direction  $\langle 1\overline{1}\overline{2}\rangle_{\gamma}$  on the  $\{111\}_{\gamma}$  plane,  $s^{\varepsilon}$  is the  $\gamma$ -austenite to  $\varepsilon$ -martensite characteristic shear, and  $\Delta f^{s,\varepsilon}$  is the increment in  $\varepsilon$ -martensite volume fraction. The characteristic shear is

$$s^{\varepsilon} = \frac{s^{tw}}{2} = \frac{1}{2\sqrt{2}} \tag{18}$$

where  $s^{tw}$  is the intrinsic twinning shear (Christian and Mahajan, 1995). Twins form by partial dislocations passing through every  $\{111\}_{\gamma}$  plane, while  $\varepsilon$ -martensite forms by partial dislocations passing through every other  $\{111\}_{\gamma}$  plane. Therefore,  $\varepsilon$ -martensite accommodates half the amount of shear strain accommodated by a twin. We found it convenient to multiply the calculated fraction by  $\beta^{DMPT} = \beta_0^{DMPT} + x_\beta(\sigma^c)K_\beta^{DMPT}$  consistent with the Olson-Cohen model to better account for the effect of triaxiality on the transformation rate. After one active slip system reached the shear band nucleation criterion (Eq. 8), all other slip systems in the same grain are assumed to also satisfy the nucleation criterion. New  $\varepsilon$ -martensite grains belonging to different slip systems are nucleated when their volume fractions reach a critical value set to  $f_{cr}^{\varepsilon} = 0.01$ . With multiple shear bands formed in the same parent austenite grain, the shear bands are assumed to span the entire parent austenite grain and intersect with each other. The newly nucleated grains inherit the state variables from the parent austenite grains and obtain crystal lattice orientation according to Eq. 10. Since the geometry of the  $\varepsilon$ -martensite grains/bands is

such that the length is much greater than the thickness, the transformed  $\varepsilon$ -martensite grains are modeled as flat ellipsoids (Feng et al., 2021).

The intersection of two shear bands is an embryo for  $\alpha'$ -martensite. Upon nucleation of a second  $\varepsilon$ -martensite shear band in a given austenite grain, the model begins considering transformation to  $\alpha'$ -martensite. For simplicity, only the  $\varepsilon$ -martensite variants of the highest SFW are selected for re-orientation into  $\alpha'$ -martensite. Additional re-orientations are included in the growth of the main  $\alpha'$ -martensite grain. Therefore, one austenite grain produces one  $\alpha'$ -martensite grain. The first  $\varepsilon$ -martensite shear band is considered to be either T/2 or T/3 shear, while the second shear band is the T/3 or T/2 shear, depending on whether T/2 or T/3 happen first. The second shear involves a search between active slip systems to find a shear that is compatible with the first shear to successfully transform into  $\alpha'$ -martensite. The second shearing is on the  $\{01\overline{1}1\}_{\varepsilon}$  planes in  $(5\overline{1}4\overline{3})_{\varepsilon}$  and  $(0\overline{1}12)_{\varepsilon}$  directions, corresponding to T/3 and T/2 shears, respectively. If more than one slip system satisfies the criterion to produce  $\alpha'$ , the one with the largest driving force is selected to reorient into an  $\alpha'$  grain inheriting the  $\gamma$  parent state variables.

The evolution of the volume fraction of  $\alpha'$ -martensite incorporating shear strain increments and characteristic shear is

$$\Delta f^{s,\alpha'} = \frac{\Delta \gamma^s}{s^{\varepsilon \to \alpha'}},\tag{19}$$

where  $\Delta \gamma^s$  is the increment in shearing strain on the HCP transformation plane,  $s^{\varepsilon \to \alpha'} = \frac{1}{3\sqrt{2}}$  is the intrinsic shear for the  $\varepsilon \to \alpha'$  transformation, and  $\Delta f^{\alpha'}$  is the increment in  $\alpha'$ -martensite volume fraction. As the volume fraction of  $\alpha'$ -martensite reaches a value of  $f_{cr}^{\alpha'} = 0.01$ , a new  $\alpha'$ -martensite grain is formed and added to the polycrystal. Subsequently, the volume fraction from  $\varepsilon$  transfers to  $\alpha'$  with shearing.

Spontaneous transformation of austenite to martensite takes place at temperature equal to or below the martensite start temperature, Ms, when  $G_{\gamma} - G_{\alpha \prime} \ge \Delta G_{crit}$ . At temperatures above Ms, spontaneous transformation is not possible due to insufficient chemical driving force,  $\Delta G_{chem}$ . At such temperatures, transformation is only possible by applying some mechanical driving force, U, i.e.  $U + \Delta G_{chem} = \Delta G_{crit}$ . In our formulation, the onset of the  $\varepsilon \to \alpha'$  transformation is driven solely by the mechanical driving force criterion

$$U^{s} = \tau^{s} \frac{T}{3} + \mathbf{\sigma}^{hyd} \cdot \mathbf{\varepsilon}^{pt,\varepsilon}, \tag{20}$$

where  $\tau^s$  is the resolved shear stress on a transformation slip system in the  $\varepsilon$ -martensite,  $\sigma^{hyd}$  is the hydrostatic stress, and  $\varepsilon^{pt,\varepsilon}$  is the phase transformation strain. The onset of  $\varepsilon \to \alpha'$  transformation begins when the mechanical driving force reaches a critical value,  $U_{cr}$ 

$$\tau^{s} \frac{T}{3} + \boldsymbol{\sigma}^{hyd} \cdot \boldsymbol{\varepsilon}^{pt,\varepsilon} = U_{cr} . \tag{21}$$

In essence, the transformation begins when the mechanical process provides enough driving force to initiate transformation. Writing the equation as

$$\tau^{s} = \frac{3U_{cr}}{T} - \frac{3}{T} \mathbf{\sigma}^{hyd} \cdot \mathbf{\varepsilon}^{pt,\varepsilon},\tag{22}$$

allows us to recognize that the right-hand side is equivalent to a slip resistance term,  $\frac{3U_{cr}}{T}$ , and a term dependent on current stress,  $\frac{3}{T}\sigma^{hyd} \cdot \boldsymbol{\varepsilon}^{pt,\varepsilon}$ . In this model,  $\frac{3U_{cr}}{T}$  is modeled as a slip resistance evolving using a hardening law, which will be described shortly.

# 2.3 Slip system hardening law

In combination with the OCPT and DMPT models, the slip system resistance evolves with shearing strain as

$$\dot{\tau}_c^s = \sum_{s'} h^{ss'} \dot{\gamma}^{s'},\tag{23}$$

where  $h^{SS'}$  is the hardening matrix consisting of partial derivatives,  $\frac{\partial \tau_c^S}{\partial \gamma^{S'}}$ , that describes the hardening effect of the slip system, s, on other slip systems, s', and  $\dot{\gamma}^{S'}$  is the shear strain-rate per slip system in a grain. The total slip resistance of a slip system in a grain consists of

$$\tau_c^s = \tau_0^\alpha + \tau_{forest}^s + \tau_{debris}^\alpha, \tag{24}$$

where  $\alpha$  indicates slip family/mode, and the terms contributing to total slip resistance are the initial nonevolving slip resistance,  $\tau_0^{\alpha}$ , and the strain hardening evolving terms with forest dislocations,  $\tau_{forest}^{s}$ , and with debris dislocations,  $\tau_{debris}^{\alpha}$ . While the initial slip resistance can explicitly include contribution from solid solution strengthening, precipitates, and grain size (Feather et al., 2019; Ghorbanpour et al., 2017), only the strain-rate and temperature effects are considered in the present formulation

$$\tau_0(\dot{\varepsilon}, T) = \tau_{0,a} \left( 1 + \tau_{0,b} \log(\dot{\varepsilon}) \right) \exp\left( -\frac{T}{\tau_{0,c}} \right), \tag{25}$$

where  $\tau_{0,a}$ ,  $\tau_{0,b}$ , and  $\tau_{0,c}$  are fitting constants. The Forest term  $\tau_{forest}^s$  accounts for the effects of statistically stored dislocations (Feather et al., 2021; Knezevic et al., 2012; Knezevic et al., 2014a)

$$\tau_{forest}^{s} = b^{\alpha} \chi \mu^{\alpha} \sqrt{\sum_{s'} L^{ss'} \rho_{tot}^{s'}},\tag{26}$$

where  $b^{\alpha}$  is the Burgers vector,  $\mu^{\alpha}$  is the shear modulus,  $\chi$  is the interaction constant,  $L^{ss'}$  is the strength interaction matrix with the interactions set to 1 (Ardeljan and Knezevic, 2018; Franciosi and Zaoui, 1982; Khadyko et al., 2016). The debris term,  $\tau^{\alpha}_{debris}$ , is driven by the debris dislocation density,  $\rho_{deb}$ 

$$\tau_{debris}^{\alpha} = 0.086 \mu^{\alpha} b^{\alpha} \sqrt{\rho_{deb}} \log \left( \frac{1}{b^{\alpha} \sqrt{\rho_{deb}}} \right). \tag{27}$$

The dislocation densities,  $\rho_{tot}^s$  and  $\rho_{deb}$ , evolve with shear strain per slip system in each grain. The total forest dislocation density evolves with shear strain, strain-rate, and temperature from an initial value,  $\rho_0^s$ , as

$$\frac{\partial \rho_{tot}^s}{\partial \gamma^s} = k_1^{\alpha} \sqrt{\sum_{s'} g^{ss'} \rho_{tot}^{s'}} - k_2^{\alpha} (\dot{\varepsilon}, T) \rho_{tot}^s. \tag{28}$$

Here,  $g^{ss'}$  is the slip system interaction matrix, assumed to be an identity matrix,  $k_1^{\alpha}$  is a fitting parameter describing the rate of dislocation generation, and  $k_2^{\alpha}$  is a derived term describing the dynamic recovery (Beyerlein and Tomé, 2008; Knezevic et al., 2015; Zecevic et al., 2020)

$$\frac{k_2^{\alpha}}{k_1^{\alpha}} = \frac{\chi b^{\alpha}}{a^{\alpha}} \left( 1 - \frac{k_B T}{D^{\alpha} (b^{\alpha})} \ln \left( \frac{\dot{\varepsilon}}{\dot{\varepsilon}_0} \right) \right), \tag{29}$$

where  $k_B$  is the Boltzmann constant,  $\dot{\varepsilon}_0 = 10^7 \text{ s}^{-1}$  is the reference strain-rate,  $g^{\alpha}$  is the normalized activation energy, and  $D^{\alpha}$  is the drag stress. And finally, the debris dislocation density evolves with shear strain, strain-rate, and temperature as (Ardeljan et al., 2016a; Knezevic et al., 2014b; Zecevic et al., 2016b)

$$\frac{\partial \rho_{deb}}{\partial \nu^s} = q^{\alpha} b^{\alpha} \sqrt{\rho_{deb}} k_2^{\alpha} (\dot{\varepsilon}, T) \rho_{tot}^s \tag{30}$$

where  $q^{\alpha}$  is a constant for the dislocation recovery rate. The initial debris dislocation density is set to a small number, 0.1 m<sup>-2</sup>.

#### 2.4 FE-EPSC

The EPSC model has been integrated into the implicit FEM framework as a UMAT in prior works (Knezevic et al., 2013; Marki et al., 2022; Zecevic et al., 2017; Zecevic and Knezevic, 2017). The EPSC model incorporating phase transformations as a UMAT is integrated here for the first time. In what follows, the subscript FE implies quantities returned/passed from the FEM solver, Abaqus. Every FE integration point of the meshes embeds the same initial texture per steel. The embedded EPSC constitutive law calculates the homogenized stress at the end of every strain increment,  $\sigma_{FE}^{t+\Delta t}$ , for a given strain increment,  $\Delta \varepsilon_{FE}$ , probing the constitutive model. The applied strain increment is driven by imposed boundary conditions over the mesh. The strain accommodated according to the EPSC model per integration point up to the current time is

$$\mathbf{\varepsilon}_{FE}^{t+\Delta t} = \mathbf{\varepsilon}_{FE}^t + \Delta \mathbf{\varepsilon}_{FE}. \tag{31}$$

In addition, the implicit coupling requires a Jacobian matrix,  $\frac{\partial \Delta \sigma_{FE}}{\partial \Delta \varepsilon_{FE}}$ , to estimate a trial displacement field. The Jacobian is (Zecevic and Knezevic, 2019)

$$\frac{\partial \Delta \sigma_{FE}}{\partial \Delta \varepsilon_{FE}} = \frac{\partial (\sigma_{FE}^{t+\Delta t} - \sigma_{FE}^{t})}{\partial \Delta \varepsilon_{FE}} = \frac{\partial \Delta \overline{\sigma}}{\partial \Delta \overline{\varepsilon}} = \frac{\partial (\overline{\mathbf{L}}^{inc} \Delta \overline{\varepsilon})}{\partial \Delta \overline{\varepsilon}} = \overline{\mathbf{L}}^{inc}.$$
 (32)

where  $\bar{\mathbf{L}}^{inc}$  is the stiffness relating the increments in Cauchy stress and strain (Zecevic and Knezevic, 2019).

#### 3. Materials and experiments

A total of five 304L stainless steels samples were examined in this study, three wrought and two AM. Table 1 summarizes mechanical tests and characterization techniques, while table 2 provides the respective chemical compositions for the studied steels. In table 1, SMARTS stands for the Spectrometer for Materials Research at Temperatures and Stress at Los Alamos National Laboratory (LANL), HIPPO stands for High Pressure Preferred Orientation time-of-flight diffractometer at LANL, and CHESS stands for the Cornell High Energy Synchrotron Source at LANL. The data acquired at CHESS is new.

Table 1. Summary of the manufacturing method, mechanical testing, and phase/texture measurement methods for the 4 types of 304L stainless steels.

Name	Manufacturing Method	Mechanical Testing	Phase Measurement		
RS1	Rolled sheet	Uniaxial tension at room temperature under various strain-rates	X-ray diffraction		
RS2	Rolled sheet	Uniaxial tension at room and elevated temperatures under a quasi-static strain-rate	In-situ neutron diffraction at SMARTS		
RB	Rolled bar, 20 mm in diameter	Torsion at 77 K under a quasi-static strain-rate	X-ray diffraction		
AM1	Laser-based AM (DMG Mori LASERTEC-65-3D)	Taylor Impact	Neutron diffraction at HIPPO		
AM2	Laser-based AM (EOS M290)  Uniaxial tension and compression + uniaxial tension of a notched specimen		Powder diffraction at CHESS		

Table 2. Chemical composition of the four 304L stainless steels used in the simulations (wt%).

	С	Cr	Ni	Si	Mo	Mn	Cu	Ti	V	P	S	N
RS1	0.028	18.13	8.32	0.45	0.15	1.32	0.26	< 0.01	0.04	0.025	0.005	0.044
RS2	0.08	19.0	9.25	0.75	0.0	2.0	0.0	0.0	0.0	0.0	0.0	0.0
RB	0.07	15.4	12.3	0.43	1.91	1.45	0.12	0.41	0.05	0.0	0.0	0.0
AM1	0.02	18.5	9.8	0.77	0.0	1.5	0.0	0.0	0.0	0.008	0.009	0.08
AM2	0.015	18.4	9.8	0.53	0.0	1.5	0.0	0.0	0.03	0.012	0.003	0.05

# 3.1 Wrought steels: simple tension data for RS1 and RS2 and torsion (shear) data for RB

Flow stress and phase fraction data for the first wrought rolled sheet (RS) material, labeled as RS1-SS304L, were presented in (Lichtenfeld et al., 2006). The sheet metal was temper rolled after heat treatment condition. The sheet had a nominal thickness of 1.5 mm and a grain size of  $\sim$ 26  $\mu$ m. Samples were cut along the rolling direction (RD) for tensile testing and pulled to fracture at ambient temperature of 25 °C under strain-rates of 1.25e-4 and 1.25 s<sup>-1</sup> on a standard

MTS system. The higher strain rate of 100 s<sup>-1</sup> was applied through an MTS 810 high strain-rate system. The samples before testing were verified to be fully austenitic. The martensite volume fraction evolution was measured using X-ray diffraction and light microscopy by stopping the tests at every 5% increments. The data in terms of volume fraction of martensite evolution and flow stress along with the modeling curves will be shown in section 4.1.

Flow stress and phase fraction data for the second wrought material, labeled as RS2-SS304L, were presented in (Wang et al., 2016). The sheet metal had an average grain size of ~25  $\mu$ m. Dog-bone tensile specimens were machined to have the tensile axis aligned with the RD and insitu neutron diffraction testing procedures were applied using the time-of-flight SMARTS instruments at LANL to measure mechanical data along with the martensite volume fractions (Bourke et al., 2002). The sample was pulled at a strain-rate of 1 e-5 s<sup>-1</sup> at room temperature and at elevated temperature of 75 °C. The data of volume fraction of martensite evolution and flow stress along with the modeling curves will be shown in section 4.1.

Since they were rolled sheets, the initial texture in the RS1-SS304L and RS2-SS304L samples was assumed as typical in such sheets. The texture is synthetically created from a random initial texture subjecting it to 60% rolling reduction while enforcing the plane strain boundary conditions using the EPSC model (Barrett et al., 2019; Eghtesad et al., 2018b; Knezevic and Landry, 2015). The synthetic texture is shown in Fig. 1a. It is used as the initial texture in simulations involving RS1-SS304L and RS2-SS304L materials.

To complement the tension data used for model calibration, we include the phase fraction data for a third wrought rolled bar (RB) material, labeled as RB-SS304L, from (Lebedev and Kosarchuk, 2000). This data is used for model validation. The material underwent torsional deformation at a cryogenic temperature of 77 K under a quasi-static strain-rate. The torsion testing was performed using an SNT-5PM hydraulic machine. The volume fraction of phases was measured using X-ray diffraction methods using a DRON-2.0 diffractometer. The initial texture for the simulation of this material was assumed to be random.

## 3.2 AM steels: simple tension/compression and impact data for AM1-SS304L and AM2-SS304L

AM technologies can lower the cost of production of low-volume components with improved properties (Bhowmik et al., 2022a; Bronkhorst et al., 2019; DebRoy et al., 2018; Ferreri et al., 2019; Ferreri et al., 2020b; Frazier, 2014; Herzog et al., 2016; Knezevic et al., 2021; Sames et al., 2016). The AM processes rely on a localized heat source such as a laser to selectively melt the metallic feedstock in the powder form and deposit the material in layers. The raw material fuses and solidifies, then the process is repeated until the desired shape and structure is formed. Different AM technologies and processing routes in each determined by process parameters can produce different microstructures including grain structures, textures, defects, and dislocation densities. This work studies two different steels and underlying microstructures created by two AM technologies, which will be labeled as AM1-SS304L and AM2-SS304L.

Manufacturing and testing of AM1-SS304L was described in (Takajo et al., 2018). A DMG Mori LASERTEC-65-3D system was used to manufacture rods to subsequently machine cylinders of 38.1 mm length and 7.62 mm diameter. These cylinders were used to perform the Taylor impact experiments. A sample launched at 235 m/s at room temperature inside a near vacuum chamber using the Taylor Anvil Gas Gun Facility at LANL was analyzed in detail. The impact facility at

LANL along with the details of its operation as well as the utility of Taylor cylinder testing was described in (Feng et al., 2022; Maudlin et al., 1999; Maudlin et al., 2003; Vasilev et al., 2020; Zecevic et al., 2016a; Zecevic and Knezevic, 2018b). The evolution of geometry, crystallographic phases, and texture was investigated and discussed. This comprehensive data used here for model validation and calibration will be presented in section 5.1. Fig. 1b shows the initial texture in the AM1-SS304L steel. The texture measurements were performed using HIPPO. For texture measurements of the deformed cylinder, the neutron beam was collimated by a 2 mm vertical slit at specific locations. Evidently, the initial material has a moderately strong  $\gamma$ -phase texture of {200} cube parallel to the build direction (BD), which is formed after the AM process. The direction is also the deformation direction.

Manufacturing and testing of AM2-SS304L was described in (Ferreri et al., 2020a; Gray et al., 2016). An Electro Optical Systems (EOS M290) laser powder bad fusion system was used to create specimens for tension and compression testing. The specimens were tested in quasi-static compression (4e-4 s<sup>-1</sup>) along with recording martensite volume fraction using an *in-situ* MTS load frame under high-energy X-ray diffraction at the Advanced Photon Source (APS). The material was also tested *ex-situ* in simple tension and compression. The data is used for modeling in the present work and will be presented in section 4.2. Fig. 1c presents pole figures showing the initial texture in the AM2-SS304L steel. In contrast to AM1, the AM2 texture exhibits {220} fiber, as a result of different manufacturing process.

In the present work, an additional test and characterization is performed for AM2-SS304L. A tensile specimen with a D-notch (the dimensions are shown in the appendix) was machined from an as-built AM2-SS304L plate using wire EDM. The D-notch was introduced in the gauge section of the specimen to promote localized damage in the illuminated volume of the material. *In-situ* powder diffraction measurements under quasi-static tension to fracture (1e-4 s<sup>-1</sup>) were performed at the F2 beamline at CHESS. The specimen was mounted on a RAMS 2 loading device (Shade et al., 2015) and *in-situ* diffraction and imaging data were collected under quasi-static tensile deformation. Micro-computed tomography (μ-CT) data were collected to characterize the initial state of the notched geometry of the specimen.

The experimental geometry for the transmission X-ray powder diffraction (XPD) measurements is shown in the appendix, where the incoming monochromatic beam of 55.618 keV with beam dimensions 1 mm x 0.05 mm (width x height) is illuminated on the gauge section of the specimen. The diffracted beam was recorded using a GE detector with a pixel size of 200 µm. *Insitu* powder diffraction data were recorded at different strain levels, as the specimen was deformed under tension. At each strain step, five different locations (see Fig. 2b) were measured by translating the sample along the z-direction (perpendicular to the incoming beam direction) and diffraction data were recorded as the sample rotated along the tensile axis. Diffraction data from 36 different projections and at five degrees integration interval (-90 to 90 degrees) and 5s exposure at each projection were recorded.

Fig. 2c shows the recorded force versus displacement for AM2 under tension during a 'stopaction' *in-situ* XPD and  $\mu$ -CT measurements. The specimen was loaded in displacement control mode and past the elastic limit, the specimen was manually unloaded (displacement reduced by 20  $\mu$ m) to prevent stress relaxation in the material during *in-situ* diffraction measurements. The sample was pulled to fracture where it reached a displacement of 0.53 mm with the displacement at ultimate tensile strength (UTS) of about 0.3 mm. The force-displacement data was measured using the load cell and crosshead available on the RAMS-2 loading device. The displacement

resolution was 100 nm. Due to the notched geometry i.e. the varying cross-section of the specimen, the force-displacement response cannot be interpreted as uniaxial as the stress state in the specimen is not uniaxial. The raw force-displacement data is plotted in Fig. 2c without a compliance correction. We have not attempted to obtain a corresponding stress-strain curve. Hence, the elastic response cannot be inferred from the curve because the response is a convolution of the material stiffness and the varying cross section in the notch. Nevertheless, whether the plastic deformation in the specimen has initiated at a given load and subsequent plasticity can be inferred. Digital image correlation was attempted on the notched sample, but due to the deep notch, there was a great deal of shadow making imaging of the speckle pattern difficult.

Fig. 2a shows force versus  $\alpha'$ -martensite volume fraction at the locations on the notched section of the sample. The data shows that the onset of transformation begins when the specimen is pulled to nearly peak load. Only austenite was measured prior to a displacement of approximatelly 0.2 mm. Interestingly,  $\alpha'$ -martensite volume at the center of the specimen, L2, is nearly 100% at fracture. Texture was also measured at L2 and will be presented later in the text. The diffraction data from 36 different projection angles allowed for the determination of the full orientation distribution function (ODF) and phase fraction of individual phases at each strain level. The sample texture was evaluated using the MAUD software (Wenk et al., 2001), which uses non-linear least squares to fit the measured data for multiple diffraction patterns to a structural model of the crystalline phases using full pattern Rietveld refinement. The corresponding phase fraction evolution of different phases present at each strain level was determined by performing Rietveld refinement using GSAS-I software (Larson and Von Dreele, 1994). Representative diffraction profiles with Rietveld refinement showing both austenite and martensite phases are provided in the appendix.

Additionally, Fig. 3 shows EBSD scans and IPF maps measured after the in-situ loading of the notched tension specimen. For EBSD, the sample preparation consisted of grinding on SiC paper with increasingly finer grit, followed by mechanical polishing with 0.3 μm alpha alumina slurry and then a mixture of 5:1 by volume of 0.04 μm colloidal silica and hydrogen peroxide (Gray et al., 2017). The scans covered 65 μm x 725 μm area with 0.2 μm step size for location 1 and 0.25 μm step size for locations 2 and 3. A ThermoFischer Scientific TM Apreo scanning electron microscope (SEM) was used for EBSD scans. The data was analyzed using EDAX TSL Orientation Imaging Microscopy (OIM) software. The approximate locations of the three EBSD scans are labeled on the undeformed sample. Estimates of the effective strain in region 2 and region 1 are approximately 0.6 and 1.0, respectively. Region 2 has trace amounts of transformed martensite, while region 1 features much higher martensite volume fraction.

Measured volume fraction of  $\alpha$ '-martensite by diffraction and EBSD during deformation of the notched specimen under tension reveals delayed onset of martensitic phase transformation in the AM2 steel. Microstructures of AM steels also feature dislocation sub-structures within grains and high dislocation density, as reported for the AM2 steel of  $\sum_s \rho_0^s = 3.81e14 \ m^{-2}$  in (Pokharel et al., 2018). The dislocation density was measured using high-resolution neutron diffraction (line profile measurements). Quantitative line profile analysis was performed using the extended Convolutional Multiple Whole Profile (eCMWP) software. The fitting procedure determines the crystallite size distribution and dislocation density. The measured powder pattern are corrected for (i) overlapping peaks, (ii) instrumental broadening, and (iii) background. The theoretical profile functions are calculated as the convolution of the theoretical size and strain

profiles and the measured instrumental profiles, and the theoretical Fourier transforms where fitted simultaneously to the normalized Fourier transforms of the corrected peaks (Ribárik et al., 2004). Dislocation sub-structures and high density of dislocations reduce the probability of shear band and stacking fault formation (Jun and Choi, 1998), which reduce the number of potential martensite nucleation sites. Moreover, the delayed transformation in the AM stainless steels is also caused by higher SFE in these steels than in wrought stainless steels (Zecevic et al., 2019). Measurements suggest the values are in the range between 15 and 20 mJ/m<sup>3</sup> for AM stainless steels (Wang and Beese, 2019; Zhu et al., 2020). The chemical heterogeneity intrinsic to the asbuilt AM steels in the form of solute micro-segregations originate from cellular and dendritic solidification in which solute atoms concentrate in cell walls and dendrite interfaces increases SFE. These cell and dendrite cores have higher SFE owing to the absence of SFE-lowering elements such as Si, Cr, and Mn (Schramm and Reed, 1975). Finally, adiabatic heating, especially under the high strain-rates like in the Taylor impact test due to short time available for heat transfer to the environment, can decrease the driving force for the austenite to martensite transformation because the SFE increases with temperature (Talonen and Hänninen, 2007). In particular, the SFW reduces with temperatures promoting cross slip, while suppressing shear band intersections, which reduces the number of martensite nucleation sites. Therefore, the nucleation of martensite reduces, the probability of closely spaced embryos at the intersection of shear bands reduces, and the coalescence of the embryos and growth of martensite reduces with temperature. In contrast, sufficient SFW at lower temperatures suppresses the cross slip and promotes the overlapping of stacking faults and formation of shear band intersections.

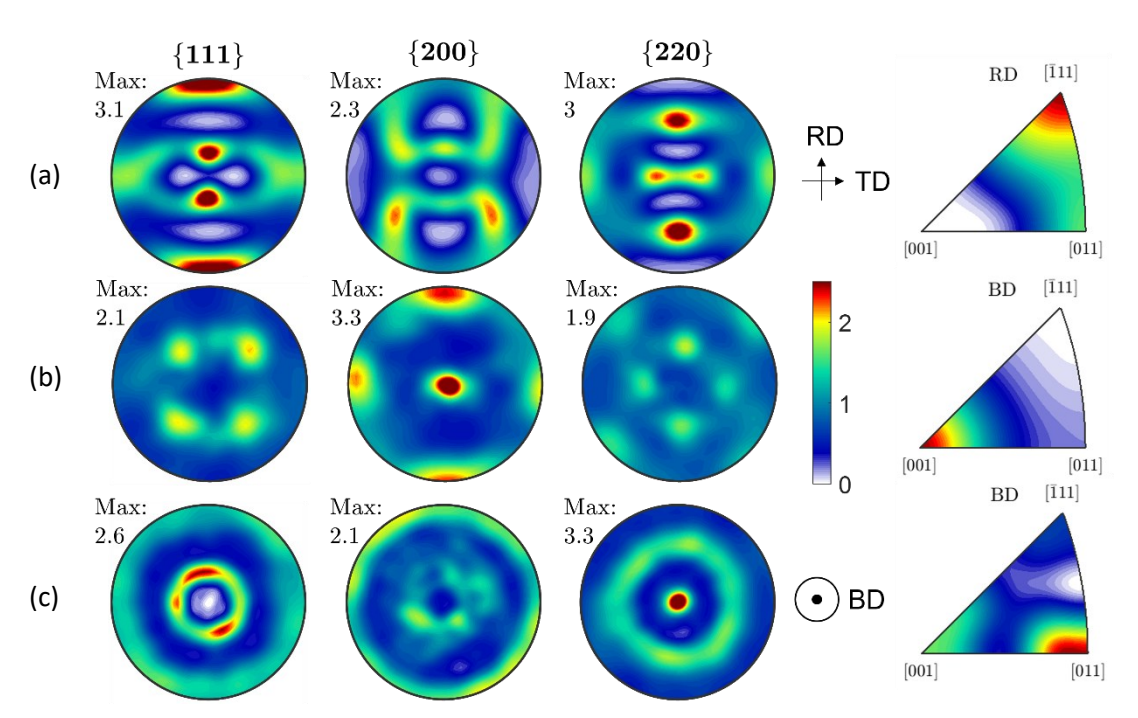


Figure 1: Pole figures and inverse pole figures showing (a) assumed initial texture for the rolled sheets (RS) of stainless steel (RS1-304L and RS2-304L) used for strain-rate and temperature sensitivity model calibration, respectively, (b) texture in the as-built AM1-304L measured by neutron diffraction and used for the Taylor impact simulation, and (c) texture in the as-built AM2-304L measured by high-energy X-ray diffraction and used for the uniaxial tension and

compression simulations including the quasi-static tension simulation of the notched specimen. Build direction (BD) is out of the plane for (b) and (c).

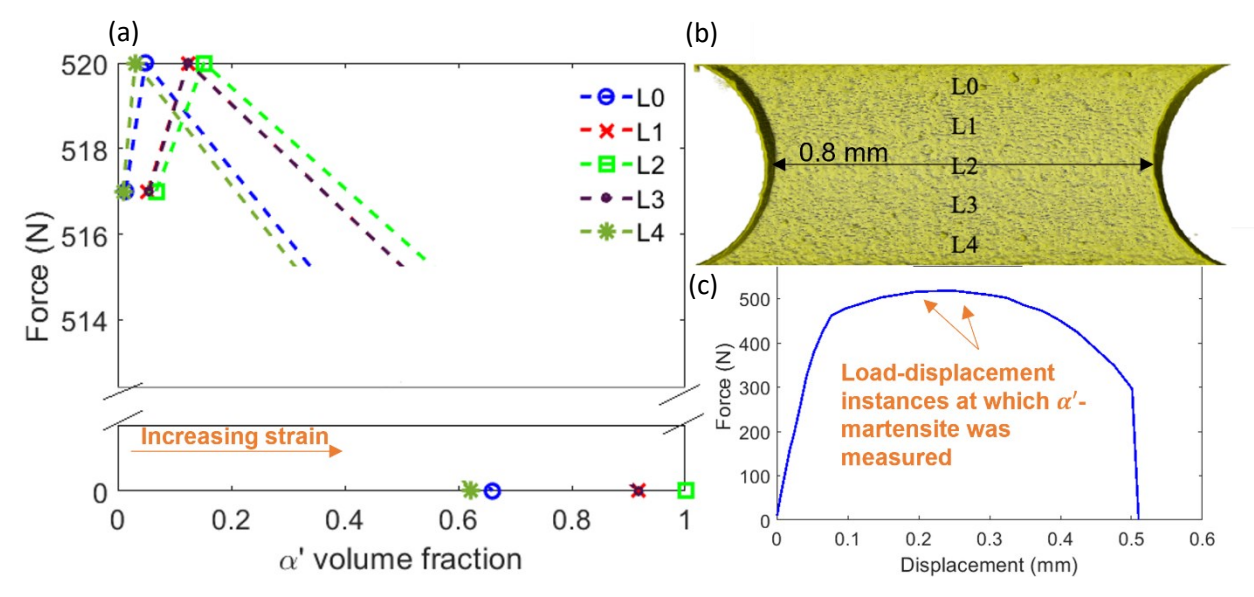


Figure 2: (a) Experimentally measured evolution of volume fraction of  $\alpha'$ -martensite at positions in the specimen as shown in (b), which is a reconstructed tomography cross section of the notched tensile specimen. (c) Force-displacement curve recorded during tension of the notched specimen at room temperature under 1e-4 s<sup>-1</sup> strain-rate. Identified positions on the force-displacement curve are points when measurements of  $\alpha'$ -martensite volume fraction took place. The third volume fraction data was measured at the end of the test.



Figure 3: Inverse pole figure (IPF) and phase maps measured after *in-situ* testing of the notched AM304L stainless steel specimen. IPF maps show local crystal orientation relative to the tensile axis, which is the build direction (BD). Regions 1, 2, and 3 on the undeformed sample

approximately identify the positions where the EBSD scans were recorded on the broken specimen after the sample was cut and polished for scanning. The grain boundaries are identified with misorientation angle greater than 5 degrees. The EBSD scans show that martensitic phase transformation of the  $\alpha'$  phase starts approximately in region 2 reaching a strain level of approximately 0.6 and forms in a high-level volume fraction in region 1, where the strain is approaching 1.0. The scale bars on the right are 30  $\mu$ m.

#### 4. Model calibration

In this section, we present the calibration and partial verification of the hardening and phase transformation laws implemented in EPSC to enable modeling of strain path, strain-rate, temperature, and microstructure and crystallographic texture dependence of martensitic transformation, while predicting the deformation behavior of 304L steels. In doing so, flow stress response, texture evolution, and phase fractions of  $\gamma$ -austenite, intermediate  $\epsilon$ -martensite, and  $\alpha$ '-martensite were calculated and compared with experimental data, while fully accounting for the crystallography of the mechanisms. The calibration is done using one element C3D8 models in Abaqus with appropriate boundary conditions.

## 4.1 Strain-rate and temperature sensitivity using RS1-SS304L, RS2-SS304L, and RB-SS304L

We begin with calibrating the hardening and OCPT laws with wrought data. The crystal elastic constants for austenite phase are  $C_{11} = 209$  GPa,  $C_{12} = 133$  GPa and  $C_{44} = 121$  GPa, while those for  $\alpha$ '-martensite phase are  $C_{11} = 234$  GPa,  $C_{12} = 135$  GPa and  $C_{44} = 118$  GPa (Wang et al., 2016).  $\{1\overline{1}1\}\langle110\rangle$  and the  $\{110\}\langle1\overline{1}1\rangle$  are slip systems used for austenite and  $\alpha$ '-martensite strain accommodation by slip, respectively. Note that the DMPT-EPSC model is identical to OCPT in terms of slip hardening so the hardening parameters are not different from those established for the OCPT-EPSC model. Note also that the hardening law parameters and the transformation laws parameters must be calibrated concurrently.

To establish the initial slip resistances (Eq. 25), we remove the strain-rate and temperature dependence by setting  $\tau_{0,b}$  to 0 and  $\tau_{0,c}$  to a large value of 1e6 such that  $\tau_0 = \tau_{0,a}$ . Then we calibrate the initial slip resistance of the austenite phase to fit the onset of yielding for each strain-rate and temperature case. After the initial slip resistances are obtained, we calculate the strain-rate and temperature sensitivities using

$$B^{\gamma} = \frac{\left(\tau_{0\varepsilon_{1}}^{\gamma}/\tau_{0\varepsilon_{2}}^{\gamma}-1\right)}{\log(\varepsilon_{1})-\left(\tau_{0\varepsilon_{1}}^{\gamma}/\tau_{0\varepsilon_{2}}^{\gamma}\right)\log(\varepsilon_{2})},\tag{33}$$

$$C^{\gamma} = \frac{-T_1 + T_2}{\log(\tau_{0_{T_1}}^{\gamma} / \tau_{0_{T_2}}^{\gamma})},\tag{34}$$

which are the ratios of Eq. (25) between the highest and lowest strain-rate and temperature cases. The resulting strain-rate sensitivity coefficient,  $\tau_{0,b}$ , for the  $\gamma$ -austenite phase is comparable to the values reported in literatures such as (Laubscher, 2012). For RS1, we only calibrated the strain-rate coefficient given the data had only strain-rate dependence. Similarly for RS2, we only calibrated the temperature coefficient. With the two coefficients determined, we simply calculate

the third coefficient  $\tau_{0,a}$ . Once the initial yield is calibrated, we proceed to adjust the remaining parameters, until all cases achieve satisfactory fits. To this end, the trapping rate coefficient,  $k_1^{\alpha}$ , drag stress,  $D^{\alpha}$  and activation barrier for de-pinning,  $g^{\alpha}$ , are identified (Daroju et al., 2022a; Daroju et al., 2022b; Savage et al., 2021). Specifically,  $k_1^{\alpha}$ , is varied such that the initial hardening slope is reproduced. Next,  $g^{\alpha}$  and  $D^{\alpha}$  are varied to reproduce the hardening rates. Finally,  $q^{\alpha}$  is established to reproduce the later stage of the hardening rates and set to  $q^{\alpha}=4$  for all simulations. For the OCPT model parameters, we refine the parameters used in the earlier work (Zecevic et al., 2019). The parameters to optimize for the OCPT law are  $\alpha_0$ ,  $K_{\alpha}$ ,  $\beta_{0,C}$ ,  $\beta_{0,n}$ , and  $K_{\beta}$ . The strain-rate formulation extended the  $\beta_0$  term, which allowed for one set of fitting parameters instead of the three case of parameters per strain-rate. Table 3 presents the established hardening parameters, while table 4 lists the established OCPT model parameters for RS1-SS304L. The comparison between measured and simulated curves is shown in Fig. 4.

Modeling of the RS2-SS304L uniaxial tension and RB-SS304L torsion data at room, elevated, and cryogenic temperatures using the OCPT model was performed in the earlier work of (Zecevic et al., 2019). We kept most of the parameters and correlated the temperature sensitivity using the  $\tau_0$  values from (Zecevic et al., 2019) with (Eq. 34). The correlation eliminated existence of multiple sets of parameters for temperature dependence. Fig. 5 shows the resulting fits of the current OCPT-EPSC model for the uniaxial tension mechanical and phase fractions data at two temperatures. Fig. 5b also includes the  $\alpha$ '-martensite volume fraction evolution predictions during torsion (simple shear) of the RB steel using RS2 parameters for model verification. While torsion induces the stress triaxiality of about zero, the phase transformations are greatly promoted because of the low temperature, 77 K.

Table 3: Hardening law parameters established for wrought RS1-SS304L and RS2-SS304L.  $\rho_0^s$  for  $\alpha'$  is inherited from the parent  $\gamma$  grain. Note that  $\tau_0$  for  $\alpha'$  is assumed to not be a function of strain-rate and temperature because the evolution of dislocation density is strain-rate and temperature sensitive.

Phase	τ <sub>0,a</sub> [MPa]	$ au_{0,b}$	$ au_{0,c}$ $[K]$	$k_1 = [m^{-1}]$	g	D [MPa]	$ ho_0^{ m s}$ $[m^{-2}]$	<i>b̂</i> [Å]	χ
$\gamma^{RS1}$	120.4	0.03	N/A	0.58 <i>e</i> 8	0.1	100	1.0 <i>e</i> 11	2.54	0.9
$\alpha'^{ m RS1}$	222.9	N/A	N/A	0.5 <i>e</i> 8	0.15	500	N/A	2.49	0.9
$\gamma^{RS2}$	241.8	N/A	264.9	0.92 <i>e</i> 8	0.24	100	1.0 <i>e</i> 11	2.54	0.9
$lpha'^{ m RS2}$	222.9	N/A	N/A	0.5 <i>e</i> 8	0.15	500	N/A	2.49	0.9

Table 4: OCPT law parameters established for wrought RS1-SS304L and RS2-SS304L.

Material	$\alpha_0$	$K_{\alpha}$	$eta_{0,C}$	$eta_{0,n}$	$K_{\beta}$	SFE	n

						$[mJ \cdot m^{-2}]$	
RS1	0.5	0.3	0.33	-0.28	1.0	5.0	2.5
RS2	0.25	0.0	12.0	0.0	0.0	5.5	2.15

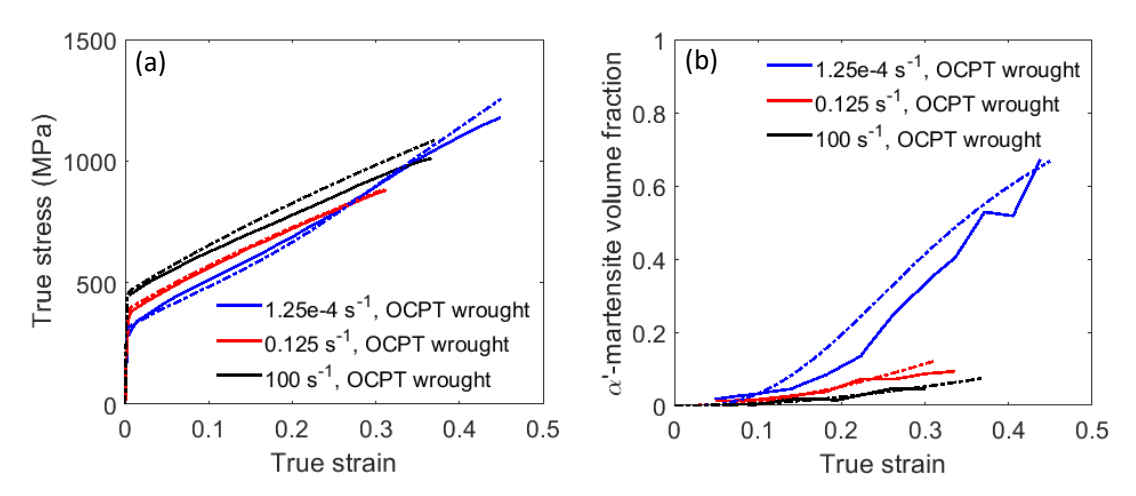


Figure 4: Comparison between measured (Lichtenfeld et al., 2006) and simulated (a) true stress-true strain response and (b) evolution of  $\alpha'$ -martensite volume fraction for wrought RS1-304L as a function of strain-rate under uniaxial tension at room temperature. Solid curves are experimental data, while the dash-dot curves are simulated data.

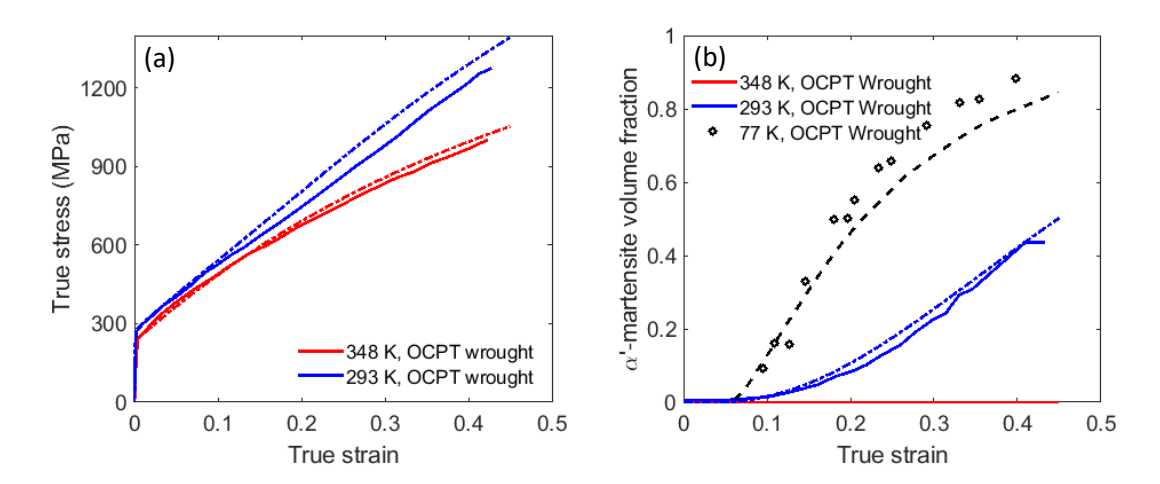


Figure 5: Comparison between measured (Wang et al., 2016) and simulated (a) true stress-true strain response at room and elevated temperatures and (b) corresponding evolution of  $\alpha'$ -martensite volume fraction for wrought RS2-SS304L under uniaxial tension at 1e-5 s<sup>-1</sup> strain-rate. Phase transformation was not observed at the elevated temperature. Solid curves are

experimental data, while the dash-dot curves are simulated data. Additionally, the black circles and black dashed curve in (b) are the experimental data and prediction, respectively, of  $\alpha'$ -martensite volume fraction evolution for the RB-SS304L steel under torsion at cryogenic temperature, 77 K.

#### 4.2 Stress state and texture sensitivity using AM1-SS304L and AM2-SS304L

Inheriting the strain-rate and temperature sensitivity from the calibration for wrought steels, we calibrated the OCPT and DMPT laws using the measured data in tension and compression for AM2-SS304L to capture the effect of stress state. Here, both models are calibrated because both are used to simulate the application case studies of the Taylor impact test and tension of the notched specimen. The fitting was performed using the multi-objective optimization scheme described in (Savage et al., 2021), which gives multiple solutions of which the most physical solution is accepted.

A notable difference between the wrought and AM materials is that the initial dislocation density in the AM austenite phase, in addition to texture. The dislocation density in the AM steels is initialized based on the measured data from (Pokharel et al., 2018). Note also that the SFE is set to a higher value for the AM materials than for the wrought materials to reflect on the measured values. Since the AM dataset do not include temperature-dependence measurements, we assume the AM material to share the same temperature coefficient,  $\tau_{0,c}$ , as the wrought material and adjusted  $\tau_{0,a}$  and the strain-rate coefficient,  $\tau_{0,b}$ . Given these constraints, the remaining parameters are calibrated to reproduce the tension and compression data. Since only monotonic tension and compression flow curves at quasi-static strain-rate and room temperature were available and the volume fraction data under compression, we have also iterated by predicting the Taylor impact test data during the calibration of the parameters. The impact test provides a wide range of strain-rates and temperatures due to the adiabatic heating for rigorous calibration for the evolution of phase fractions. Therefore, the strain-rate sensitivity from the wrought steels was slightly refined to better fit the data. The macroscopic strain-rate sensitivity originating from the established parameters was found to have a significant effect on the deformed geometry of the Taylor impact cylinder and was adjusted from 0.03 as calibrated for the wrought materials to 0.056 for the AM materials. Therefore, the AM steels are more strain-rate sensitive than the wrought steels, which will be discussed in section 5.1. Note that the same values for the hardening parameters are used for AM1 and AM2 materials. Only, one additional set of hardening parameters is established for the  $\varepsilon$ -martensite phase. The  $\varepsilon$ -martensite parameters have the same values used in the previous study (Feng et al., 2021), except the initial slip resistance since the AM steels are stronger than wrought steels. Moreover, the added parameters for the advanced DMPT law are the phase transformation parameters  $K_{\beta}^{DMPT}$  and  $\hat{\beta}_{0}^{DMPT}$ . The slip systems in the  $\varepsilon$ -martensite are restricted to pyramidal slip on  $\{01\overline{1}1\}_{\varepsilon}$  planes in  $\langle 5\overline{1}4\overline{3}\rangle_{\varepsilon}$  and  $\langle 0\overline{1}12\rangle_{\varepsilon}$  directions to facilitate the  $\varepsilon \rightarrow \alpha$ ' transformation. The initial slip resistances for the transformed phases are assumed to not depend on strain-rate and temperature since their transformation occurs at a late stage of the deformation and the dislocation density (inherited from the previous austenite) is dependent on strain-rate and temperature. The crystal elastic constants for  $\varepsilon$ -martensite are  $C_{11}=268.7~GPa, C_{12}=128.6~GPa, C_{13}=77.67~GPa, C_{33}=$ 319.7 GPa and  $C_{44} = 49.26$  GPa (Fellinger et al., 2019; Pronk and Frenkel, 2003). The calibrated parameters are listed in table 5 – table 8, and the comparison between the measured

and simulated curves are shown in Fig. 6. The effect martensite transformations on the flow stress presented in Fig. 6 was small in the early portion of deformation because of the delayed onset of transformation in the AM materials. While the calibration portions for tension and compression in Fig. 6 are to about 0.5 strain and 0.1 strain, respectively, the curves are extrapolated to 1.0 strain for subsequent modeling of the notched tension specimen and impact to larger strains. The extrapolation is therefore validated by predicting the behavior and microstructural evolution of the notched tension specimen and Taylor cylinder in later sections. Given that the hardening would approach saturation to a steady state and also that austenite phase would nearly fully transform into  $\alpha$ '-martensite at slightly large strains than 1.0, the model validity in even a wider range of true strains such as those encountered in severe plastic deformation processes is likely, but such validation is left for future works. The AM steels are significantly stronger than wrought steels because of dislocation density and underlying dislocation structures inducing the Hall-Petch barrier effect. Formation of shear bands of sufficient width and their intersection as required for the martensite nucleation is difficult in such fine structures. This is in contrast to the coarse grained wrought austenitic steels in which a large number of shear band intersections are available for the nucleation of martensite and subsequent growth of nucleus, which lead to high fraction of martensite.

The stress-strain response under transformation induced plasticity is a consequence of multiple phenomena. Based on the kinematics of the martensitic transformation, the volume change associated with phase transformation should elongate a material point undergoing the martensitic transformation. As martensite grains are created and growing with transformation, these grains deform elastically because martensite has higher activation resistance for slip than austenite. This localized elastic deformation is increasing the stress very rapidly with further straining. As a result, there is a change in the hardening rates going from FCC austenite to HCP  $\varepsilon$ -martensite to BCC  $\alpha$ '-martensite due to the underlying changes in the geometry of slip systems, their slip resistances, and local dislocation density. The intermediate  $\varepsilon$ -martensite phase significantly hardens the material due to its hexagonal structure and underlying deformation mechanisms. As seen in the figure,  $\gamma \to \varepsilon$  transformation during tension is more rapid and substantial than during compression for the studied steels. Furthermore, the fraction of austenite grains that form  $\varepsilon$ martensite phase during tension transforms more rapidly into  $\alpha$ '-martensite than those during compression. Therefore, the hardening effect is more pronounced in tension than in compression. In summary, the underlying reasons for a slightly progressive stress-strain response starting exactly at the point where the volume change associated with phase transformation should elongate the transforming volume are the transformation induced hardening phenomena.

Table 5: Hardening law parameters adjusted for AM1-SS304L and AM2-SS304L.  $\rho_0^s$  for  $\alpha'$  is inherited from the parent  $\gamma$  grain. Note that  $\tau_0$  for  $\alpha'$  is assumed not a function of strain-rate and temperature because the evolution of dislocation density is strain-rate and temperature sensitive.

Phase	$ au_{0,a}$ $[MPa]$	$ au_{0,b}$	$ au_{0,c}$ [K]	$k_1 \\ [m^{-1}]$	g	D [MPa]	$ ho_0^{ m s} \ [m^{-2}]$	<i>b</i> [Å]	χ
γ	286.2	0.056	240.8	5.0 <i>e</i> 8	0.05	200	3.18 <i>e</i> 13	2.54	0.11

lpha'	222.9	N/A	N/A	5.0 <i>e</i> 8	0.15	500	N/A	2.49	0.11
		,	,				,		

Table 6: OCPT law parameters for AM1-SS304L and AM2-SS304L.

$\alpha_0$	$K_{\alpha}$	$eta_{0,C}$	$eta_{0,n}$	$K_{eta}$	$SFE$ $[mJ \cdot m^{-2}]$	n
1.343	1.369	0.33	-0.18	4.163	17.0	4.0

Table 7: Hardening law parameters adjusted for AM1-SS304L and AM2-SS304L.  $\rho_0^s$  for  $\varepsilon$  and  $\alpha'$  are inherited from the parent  $\gamma$  grain. Note that  $\tau_0$  for  $\varepsilon$  and  $\alpha'$  is assumed not functions of strain-rate and temperature because the evolution of dislocation density is strain-rate and temperature sensitive.

Phase	$ au_{0,a}$ [MPa]	$ au_{0,b}$	$ au_{0,c}$ $[K]$	$k_1$ [ $m^{-1}$ ]	g	D [MPa]	$ ho_0^{ m s} \ [m^{-2}]$	<i>b</i> [Å]	χ
γ	286.2	0.056	240.8	5.0 <i>e</i> 8	0.05	200	3.18 <i>e</i> 13	2.54	0.11
ε	300	N/A	N/A	0.21 <i>e</i> 8	1e6	100	N/A	1.47	0.11
lpha'	222.9	N/A	N/A	0.5 <i>e</i> 8	0.15	500	N/A	2.49	0.11

Table 8: DMPT law parameters for AM1-SS304L and AM2-SS304L.

${\alpha'}_{int}$	$f_{arepsilon}^{cr}$	$f_{lpha'}^{cr}$	$SFE$ $[mJ \cdot m^{-2}]$	$K_{oldsymbol{eta}}^{DMPT}$	$eta_0^{DMPT}$
1.0	0.01	0.01	17.0	1.4	0.53

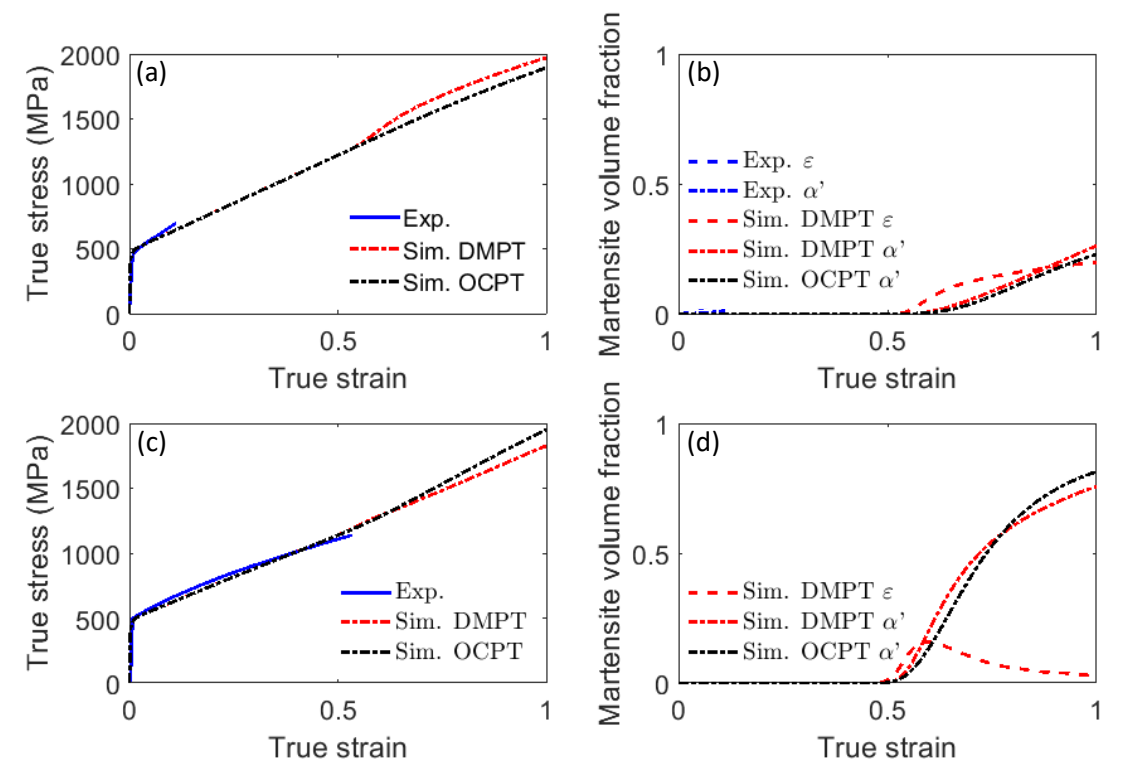


Figure 6: Comparison of experimentally measured and simulated ((a), (c)) true-stress-true-strain curves and ((b), (d)) martensite volume fraction evolution for AM2-SS304L under room temperature and 1e-4 s<sup>-1</sup> strain-rate, subjected to ((a), (b)) simple compression and ((c), (d)) simple tension. The experimental curves were not deformed to fracture. Both  $\varepsilon$ - and  $\alpha'$ -martensite volume fractions were measured for compression data while volume fraction evolution for uniaxial tension was not measured.

Since they are based on similar crystallographic formulations, both OCPT and DMPT models provide similar predictions in terms of the phase fractions. The DMPT model predicts that  $\gamma \to \varepsilon$ transformation during tension is more rapid and substantial than during compression. After an initial increase of  $\varepsilon$ -martensite fraction, the  $\varepsilon \to \alpha'$  transformation begins, decreasing the rate of  $\varepsilon$ -martensite fraction evolution. The model predicts that the fraction of austenite grains that form  $\varepsilon$ -martensite phase during tension transforms more rapidly into  $\alpha$ '-martensite than those during compression. The volume fraction of  $\varepsilon$ -martensite is decreasing in tension, meaning that the rate of  $\varepsilon \to \alpha'$  transformation is greater than the rate of  $\gamma \to \varepsilon$  transformation. The stress state in grains and respective crystal orientations influence the separation between partials on active slip systems and determine whether the grain will form  $\varepsilon$ -martensite (Zecevic et al., 2019). The stress state affects the slip resistance according to Eq. (22). Accordingly, the slip resistance for  $\varepsilon$ martensite is lower for tension ( $\sigma^{hyd} \cdot \boldsymbol{\varepsilon}^{pt} > 0$ ) than compression ( $\sigma^{hyd} \cdot \boldsymbol{\varepsilon}^{pt} < 0$ ). Given the initial texture of the AM2-SS304L steel, the process of separation between partials is more effective in tension than compression. The DMPT model relates the martensite fraction with the shear strain on the active slip systems in each grain. Therefore, the fraction of martensite depends on the crystal lattice orientation with respect to the loading direction and resulting stress state in the crystal. The transformation propensity is at the maximum for (011) grains parallel to

the tensile direction (Burgers and Klostermann, 1965; Goodchild et al., 1970; Lagneborgj, 1964; Petit et al., 2007). In contrast, the <001> grains parallel to the compression direction have the highest propensity to transform, while <011> grains have minimal propensity to transform in compression (Goodchild et al., 1970).

Fig. 7 compared the calibrated values of the initial slip resistance as functions of strain-rate and temperature using both laws for wrought and AM steels. For these comparisons, the varying strain-rate cases are simulated at room temperature while the varying temperature cases are simulated at quasi-static 1e-4 s<sup>-1</sup>. Although the trends are similar, the wrought materials exhibit reduced strength, as expected. The established parameters will be used in the next section for the two application case studies to further illustrate their validity and the modeling framework utility.

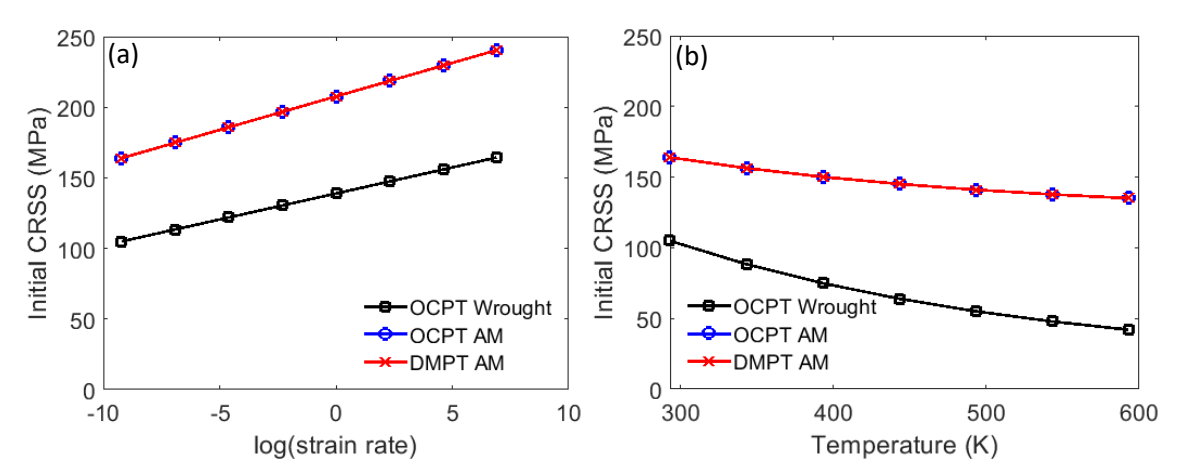


Figure 7: (a) Strain-rate sensitivity and (b) temperature sensitivity of the initial critically resolved shear stresses (CRSS). The varying strain-rate simulations are at a temperature of 293 K, while the varying temperature simulations are at a strain-rate of 1e-4 s<sup>-1</sup>.

#### 5. Results and discussion

The OCPT and DMPT laws within the FE-EPSC UMAT are used to provide the constitutive relationship between stress and strain at FE integration points in the simulation of the Taylor impact test and of tension of the notched specimen. While the formulations of the phase transformation laws are advanced incrementally, the most critical contribution of the present work is the experimental validation of the integrated crystal plasticity-based simulation framework for predicting microstructural evolution and geometric shape changes of stainless steels. Through the applications we show that, in addition to being predictive with great accuracy, the key advantage of the FE-EPSC framework lies in its versatility.

## 5.1 Taylor impact of AM1-SS304L steel

Since the polycrystalline AM1-SS304L exhibits the statistical sample symmetries of orthotropic type (Fig. 1b), we model a quarter of the cylinder. The simulation setup for the Taylor impact

test is shown in Fig. 8. The setup is mirrored as a full cylinder for a visual presentation of the model. The model's z-direction aligns with the build direction (BD) of the texture in Fig. 1b. Mesh sensitivity study was performed to reduce the mesh to 384 linear hexahedral (C3D8) elements, partitioned to have the elements near the foot of the cylinder be 1/4 the size of the elements near the tail of the cylinder. Along with the x and y symmetry boundary conditions, a z-direction velocity boundary condition of 235 m/s are imposed on the model. The simulation runs to a total time of  $100 \, \mu s$ . The simulated deformed cylinder fully separates from the surface at  $73.4 \, \mu s$ .

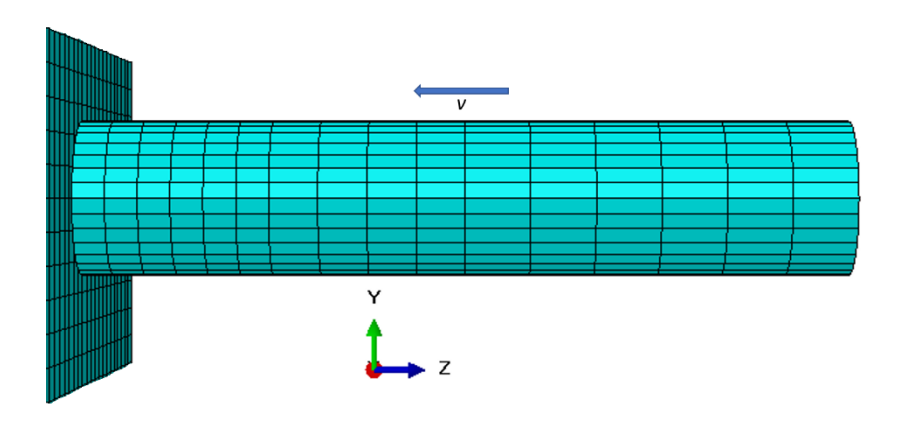


Figure 8: FEM model used for the Taylor impact simulation in Abaqus. The cylinder is mirrored as a full model for a visual presentation from a quarter model consisting of 384 C3D8 elements. A velocity boundary condition of 235 m/s was applied. The impact direction aligns with the build direction of the sample.

Fig. 9 presents comparisons between simulation results and experimental measurements taken from (Takajo et al., 2018) in terms of capturing the evolution of geometry and phases. Fig. 9a compares the cylinder radius. The FE-EPSC with the OCPT law predicts a slightly softer material as the foot is more deformed than the FE-EPSC with the DMPT law. The DMPT law evolves the intermediate  $\varepsilon$ -martensite phase that due to its hexagonal structure and underlying deformation mechanisms hardens the material. Larger strain in the material predicted by OCPT than DMPT causes more transformation. Therefore, the final  $\alpha'$ -martensite volume fraction predicted by the OCPT law is slightly higher than that predicted with the DMPT law, as shown in Fig. 9b. Nevertheless, both OCPT and DMPT laws predict well the general trend of the martensite volume fractions along the cylinder. The measured volume fraction of  $\varepsilon$ -phase in the sample was up to 0.6% between 20- and 25-mm distance from the foot and negligible amounts elsewhere. The DMPT predicts less than 0.5% near the foot and 0.2% between 15- and 20-mm of  $\varepsilon$ -martensite along the cylinder. In summary, the models predicted the evolution of geometry and phases as functions of strain level, strain-rate, and temperature. In particular, the competing effects of strain level promoting the transformation and temperature increase suppressing the transformation are predicted as adiabatic heating decreases the driving force for the austenite to martensite transformation. One of the known limitations of the OCPT law is its inability to predict saturated fraction of martensite. As a result, it overpredicts the fraction of martensite in the foot region.

As the deformation process subjects the cylinder to variable strain-rates of up to 460,278 s<sup>-1</sup>, hardening rates also vary significantly. Figure 10 shows the simulated Taylor impact process highlighting the propagation of equivalent plastic strain-rate fields at every 9 µs of the simulation. While the highest strain-rate of 460,278 s<sup>-1</sup> is observed during the onset of the impact at 0.703 µs, the third time frame shows relatively high strain-rates between 5- and 15-mm where the rebound shockwave combines with the forward shockwave and resulted in the second "shoulder" on the deformed cylinder. Then, the shockwave dissipates and the cylinder separates from the anvil at 73.4 µs. When using the strain-rate sensitivity value of 0.03 calibrated for the wrought steels, the simulations over predicted the curvature of the cylinder between 5- and 15-mm due to much more deformation. As explained earlier, we have adjusted the strain-rate sensitivity for the AM steels to predict the deformed geometry. The calibrated value of 0.056 resulted in geometries that matched well with the measured values.

Fig. 11 shows the strain and temperature contour fields at the end of deformation using the FE-EPSC with DMPT model. Contours predicted by the FE-EPSC with OCPT model are very similar and are not provided. The highest strains are observed at the foot of the cylinder and between 5- to 15-mm matching the deformed geometry. At the foot where the stress is also higher, the model predicts the highest temperature increase of up to 329 K from room temperature. The current temperature is updated by (Goetz and Semiatin, 2001):

$$T^{t} = T^{t-1} + \Delta T^{t} = T^{t-1} + \eta \frac{\Delta W^{\text{pl},t}}{\rho c_{\text{p}}},$$
(35)

where  $\Delta W^{\mathrm{pl},t} = \mathbf{\sigma}^t$ :  $\dot{\mathbf{\epsilon}}^{\mathrm{vp},t}$  is the plastic work increment calculated with the stress,  $\mathbf{\sigma}^t$ , and the viscoplastic strain-rate,  $\dot{\mathbf{\epsilon}}^{\mathrm{vp},t}$  at the beginning of the current strain increment, t. Parameter  $\eta$  is the thermomechanical conversion factor (or Taylor-Quinney coefficient) set to 0.95.  $\rho$  is the density and  $C_{\mathrm{p}} = 0.5 \frac{J}{gK}$  is the specific heat capacity of 304L stainless steel.

Figs. 12 and 13 present the evolution of  $\varepsilon$ -martensite and  $\alpha'$ -martensite, respectively, during the Taylor impact simulation. The simulation times are chosen to show an increase and then a decrease of the  $\varepsilon$ -phase volume fraction and finally the monotonic increase of the  $\alpha'$ -phase volume fraction. Since the majority of the deformation and transformation occurs during the onset of the impact, the most representative times chosen are 3.5  $\mu$ s and 4.2  $\mu$ s. The volume fraction contour fields at the end of the simulation are also shown as reference.

Fig. 14 shows the comparison between measured and simulated of texture evolution along the cylinder. The predicted textures are exported from elements at the given distance consistent with the experimental measurements. Evidently, the heavy deformation in the foot region changed the initial {200} parallel to the BD and the deformation direction to {220}, consistent with compression of FCC metals (Kocks et al., 1998).

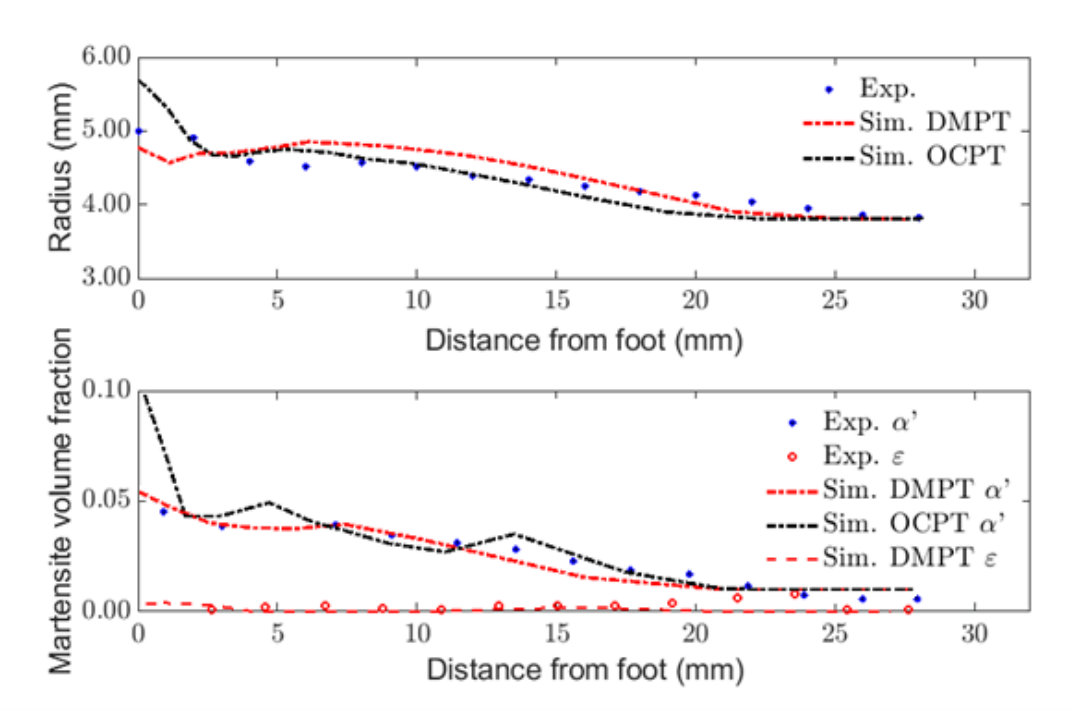


Figure 9: Comparisons of measured and simulated (a) Taylor impact cylinder radius and (b) martensite volume fraction along the cylinder after the impact predicted using FE-EPSC with either OCPT or DMPT.

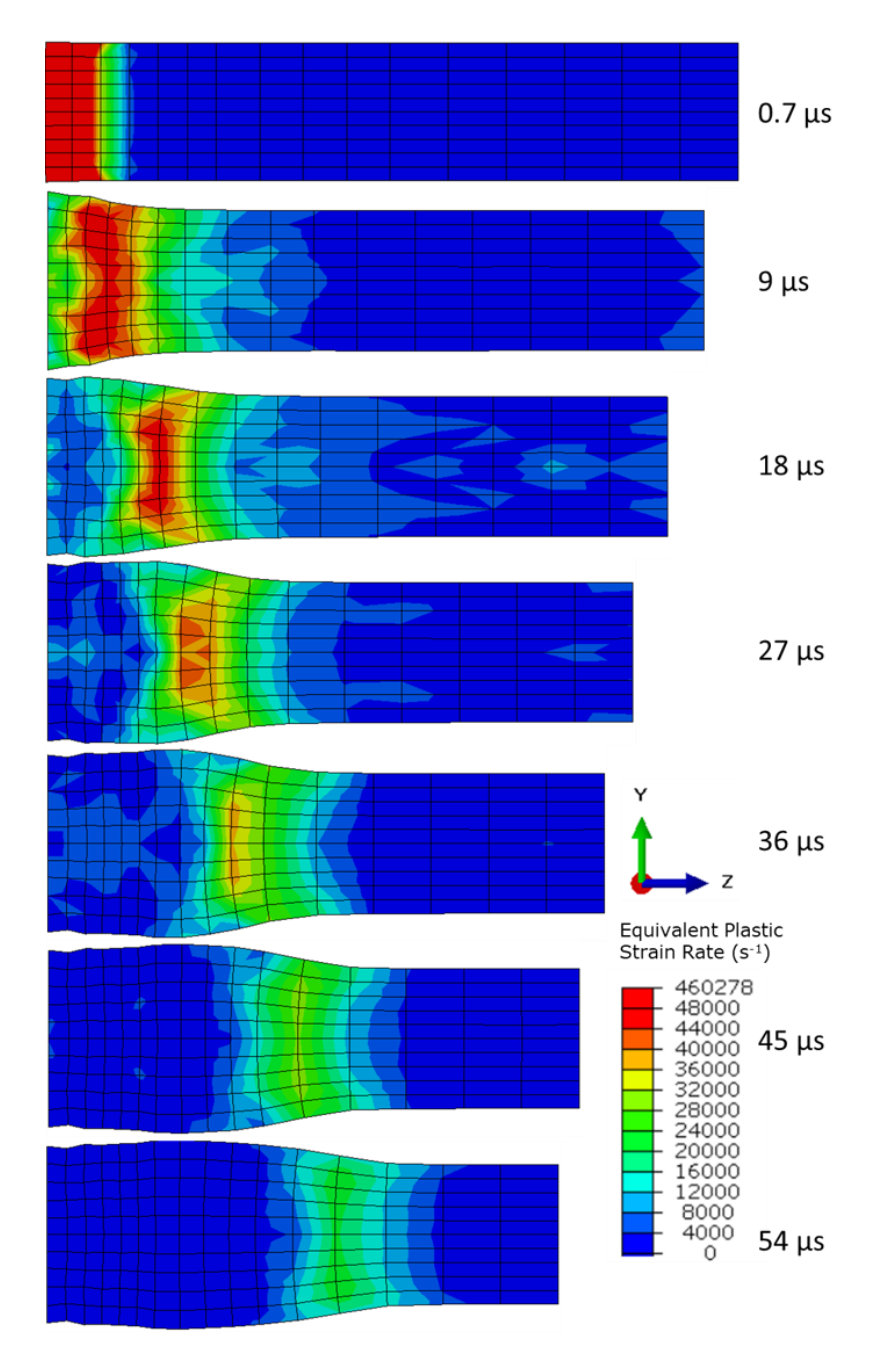


Figure 10: Plastic strain-rate propagation through the projectile with time as predicted using FE-EPSC with DMPT model. The model is mirrored in the x-z plane as a half cylinder for visual presentation. The legend limits of all frames are conveniently unified between 0 to 48,000 to highlight the location of the highest strain-rate in each time frame. The values higher than the range take the same color as the maximum in the range. The maximum simulated strain-rate during the whole simulation is  $460,278 \text{ s}^{-1}$  at  $0.703 \mu s$ .

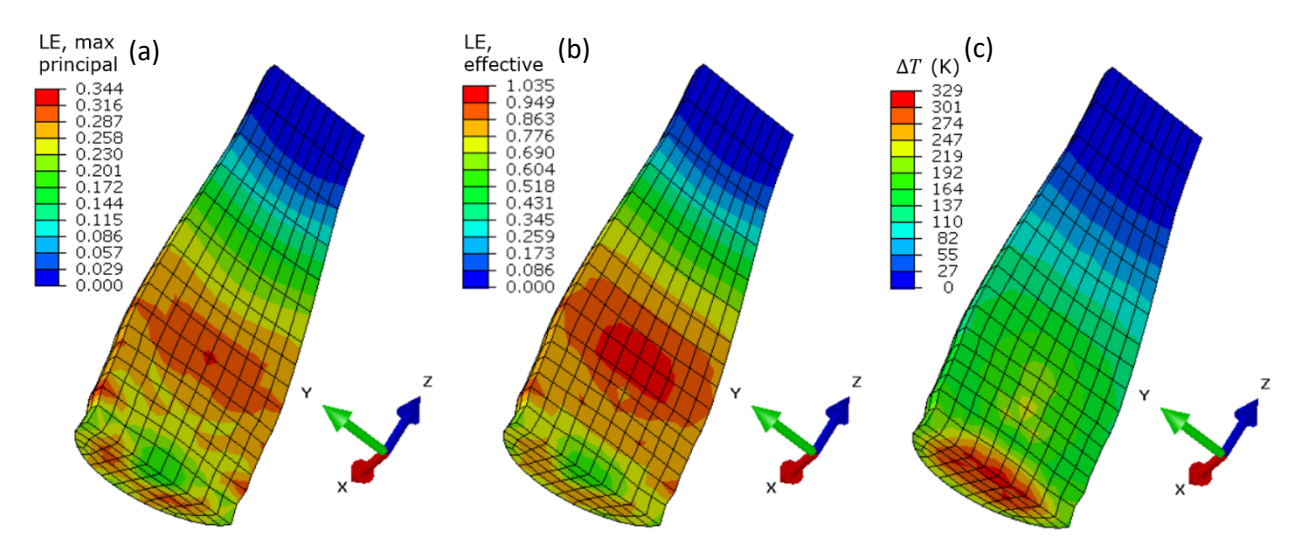


Figure 11: Contour fields showing (a) maximum principal true strain, (b) effective true strain, and (c) temperature increase at the end of the Taylor impact simulation using the FE-EPSC with DMPT model. The model is mirrored in the x-z plane as a half cylinder for visual presentation.

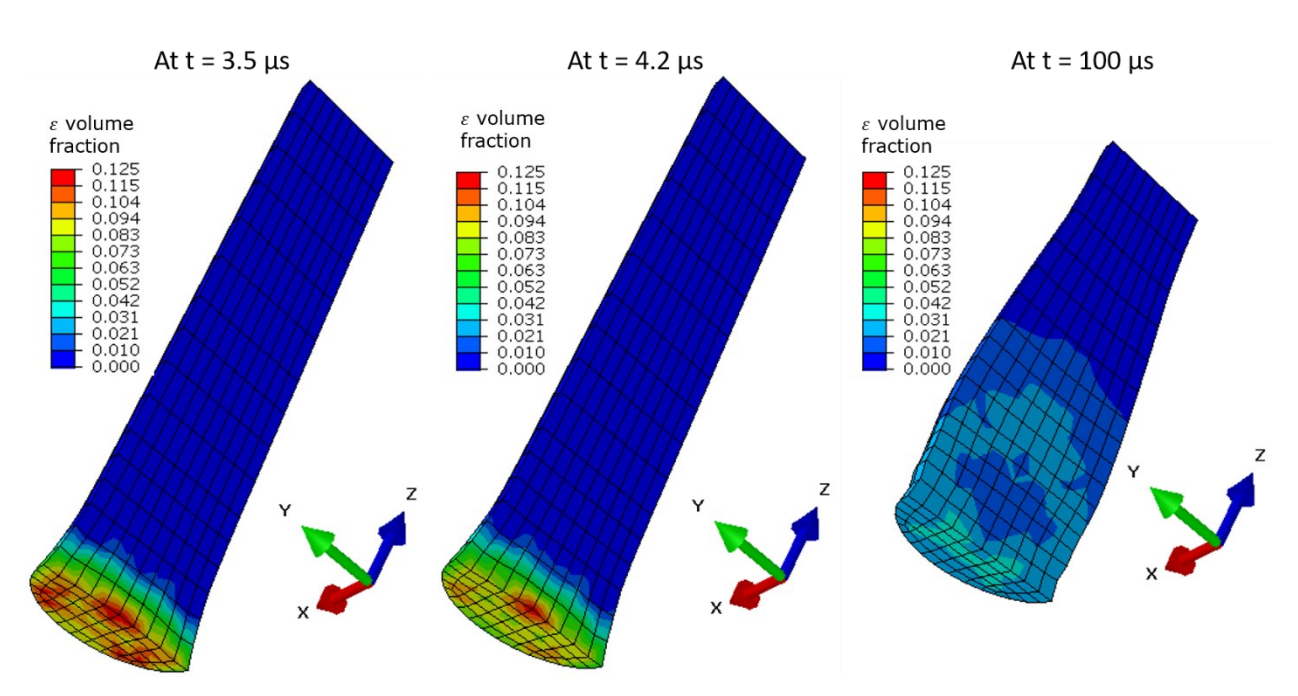


Figure 12: Spatial fields showing the evolution of  $\varepsilon$ -martensite volume fraction over the mesh at 3 select simulation time instances for the Taylor impact simulation using the FE-EPSC with DMPT model. The contours highlight an increase and then a decrease of  $\varepsilon$  phase volume fractions as  $\varepsilon$  transforms to  $\alpha'$  with time/strain.

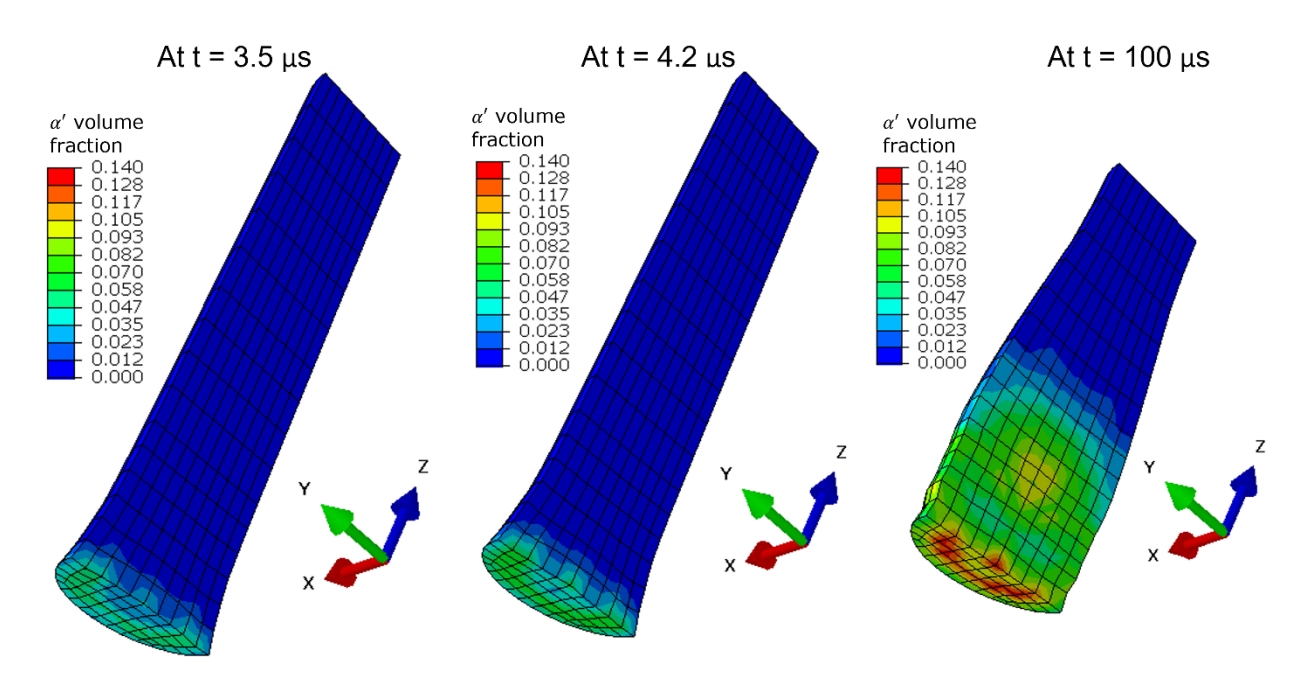


Figure 13: Spatial fields showing the evolution of  $\alpha'$ -martensite volume fraction over the mesh at the same 3 simulation times as in figure 11 for the Taylor impact simulation using the FE-EPSC with DMPT model. The contours show increase of  $\alpha'$  phase with time/strain.

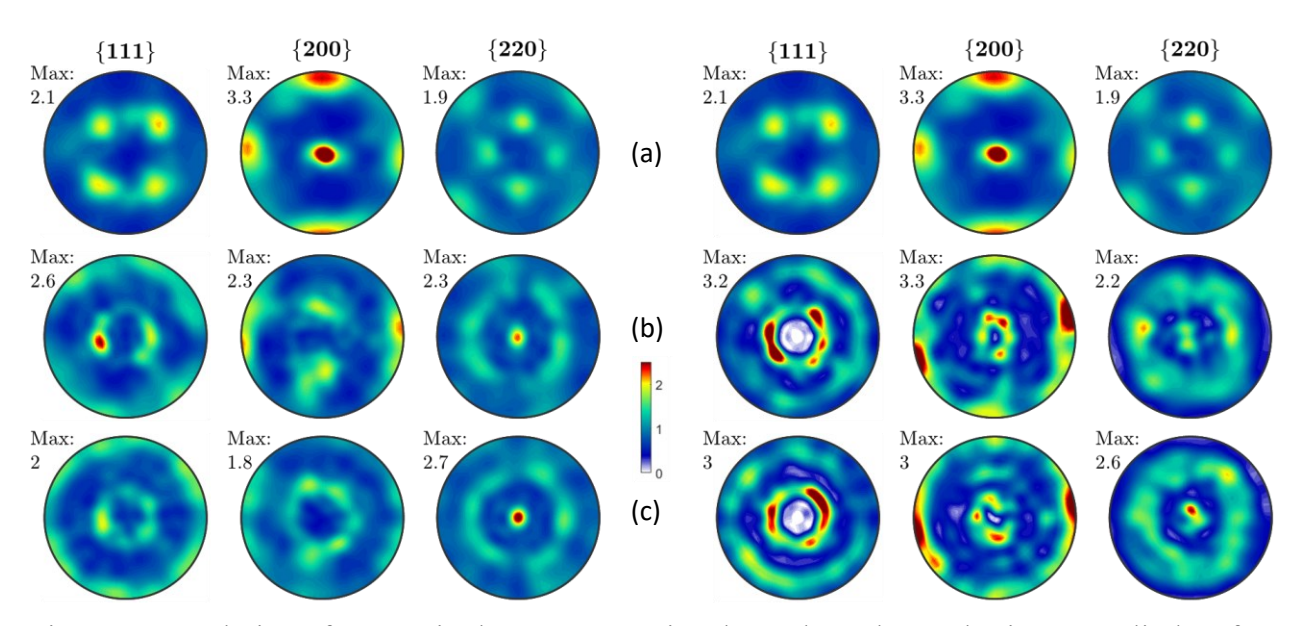


Figure 14: Evolution of texture in the FCC austenite phase along the Taylor impact cylinder after the impact: (a) at the undeformed tail (28 mm from the foot), (b) in the middle of the cylinder (14 mm from the foot), and (c) at the foot. Measured textures by neutron diffraction are on the left, while predicted textures are on the right. The build direction is at the center of pole figures.

## 5.2 Tension of notched specimen of AM2-SS304L steel

Utilizing the polycrystalline AM2-SS304L steel sample symmetry, we model an eighth of the notched section of the tension specimen as shown in Fig. 15. The model imposes x, y, and z symmetries on the inner -x, -y, and -z surfaces, a displacement boundary condition in the z-direction on the +z surface, and free lateral surface i.e., the +x and +y surfaces to ensure simple tension boundary conditions. Since the model has symmetry in the z-direction, the imposed displacement is slightly more than half of the measured displacement at UTS, since the model does not simulate material failure.

As the modeled section is thin in the z direction in comparison to the cross section, the hourglass effect is not significant given the number of elements in the z-direction, so reduced integration point elements were used to decrease computation time from 54.12 hours for the full integration to 10.38 hours for the reduced integration on a 16 2.10 GHz Intel Xeon(R) Gold 6130 CPUs workstation. Following a mesh sensitivity study, the mesh is reduced to 600 linear hexahedral reduced integration (C3D8R) elements.

Fig. 16a compares the simulated and measured force displacement curves. The force displacement curves from both OCPT and DMPT show good agreement with the measured forces during plastic deformation and near fracture. Simulation results of  $\alpha$ '-phase volume fraction in Fig. 16b show slightly high transformation rate than measured. The volume fraction value at locations L1 and L2 are extracted from the elements at locations corresponding to L1 and L2, i.e., top and bottom elements along the center of the mesh. Since the third measured volume fraction data points are at fracture, the model does not reach those point as the fracture is not modeled. Fig. 16c compares the simulated and measured displacement versus  $\alpha'$ -martensite volume fraction. Here, the difference between OCPT and DMPT curves is visible. Since DMPT evolves the  $\varepsilon$ -martensite and begins earlier, it also transforms  $\alpha'$ -martensite earlier. However, both models predict the trends that are reasonably in agreement with the data.

Fig. 17 presents the contours of effective true strain, triaxiality, and von Mises stress on the deformed notched specimen. The effective strain reaches about 1.31 at the notched edges. This matches with the von Mises stress contours that also show similar stress concentrations at the sharp edges. The triaxiality contours match well with the stress contours and the predicted  $\alpha'$ -martensite volume fraction contours. The higher intensity at the corners is due to stress concentrations due to the notched geometry. Although the strain and stress values are similar between locations L1 and L2, the overall stress and strain on the layer containing L2 is higher than the layer containing L1 due to these concentrations.

Fig. 18 presents the evolution of  $\varepsilon$ -martensite volume fraction at even displacement levels during the tension simulation. The contour plots show the increase then decrease of the  $\varepsilon$ -martensite phase volume fraction as  $\varepsilon$ -martensite transforms into  $\alpha'$ -martensite monotonically. The legend maximum and minimum values are set to highlight this trend. Fig. 19 shows the monotonic evolution of  $\alpha'$ -martensite volume fraction at the same displacement levels, showing the volume fraction approaching 1.0 along the edges where stress and strain are concentrated.

Fig. 20 compares the experimentally measured textures (Ferreri et al., 2020a) with the simulated textures. The simulated textures are extracted from the element corresponding to location L2 on the deformed model as a representative texture for the region. The predicted and measured deformed FCC textures both show an increase of the {200} intensity from an initial pole in {220} and the formation of distinct "ring" patterns in {111} and {220} pole figures. The

martensite textures are mainly due to transformation and deformation, and, to a smaller extent, are similar to those presented in (Feng et al., 2021; Zecevic et al., 2019).

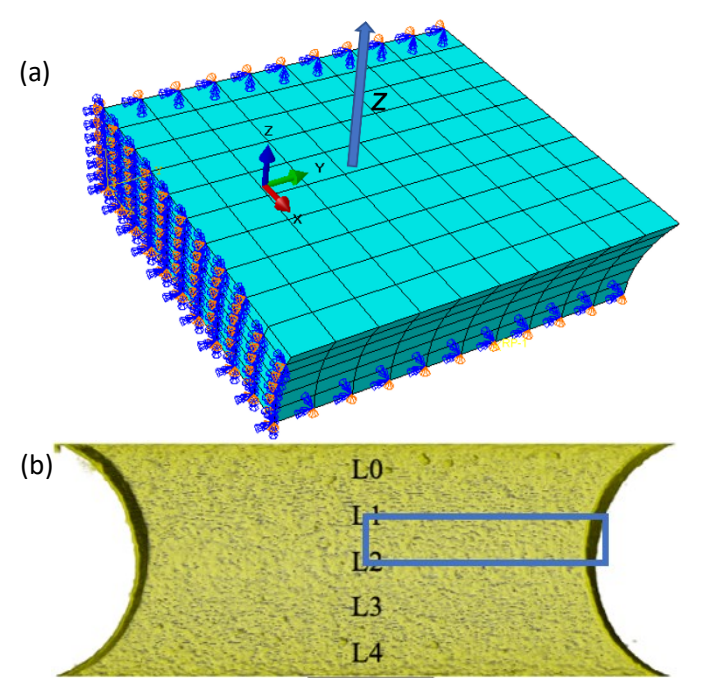
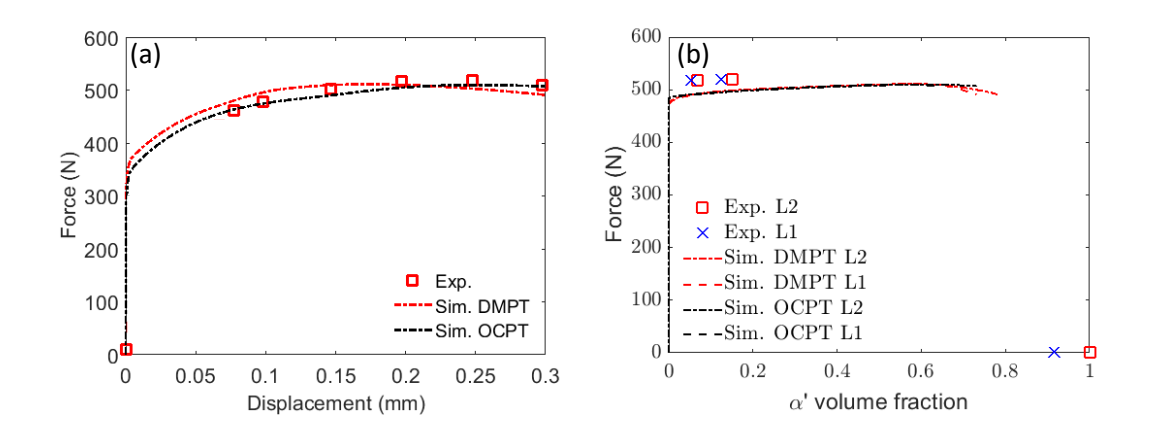


Figure 15: (a) FE mesh consisting of 600 C3D8 elements along with symmetry boundary conditions for uniaxial tension simulation along the z-direction in Abaqus. (b) Tomographic reconstruction showing the section of the notched tension specimen modeled in Abaqus.



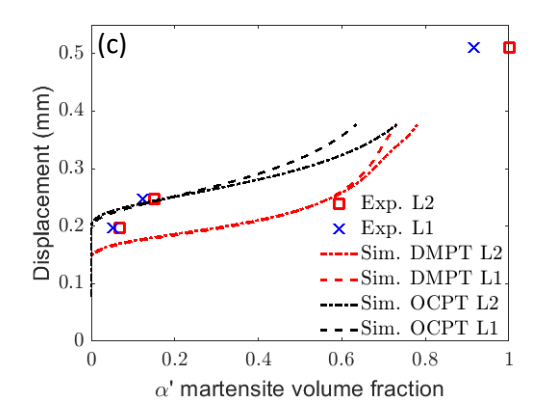


Figure 16: Experimental and simulated (a) force versus displacement, (b) force versus  $\alpha'$ -martensite volume fraction evolution, and (c) overall displacement versus  $\alpha'$ -martensite volume fraction evolution.

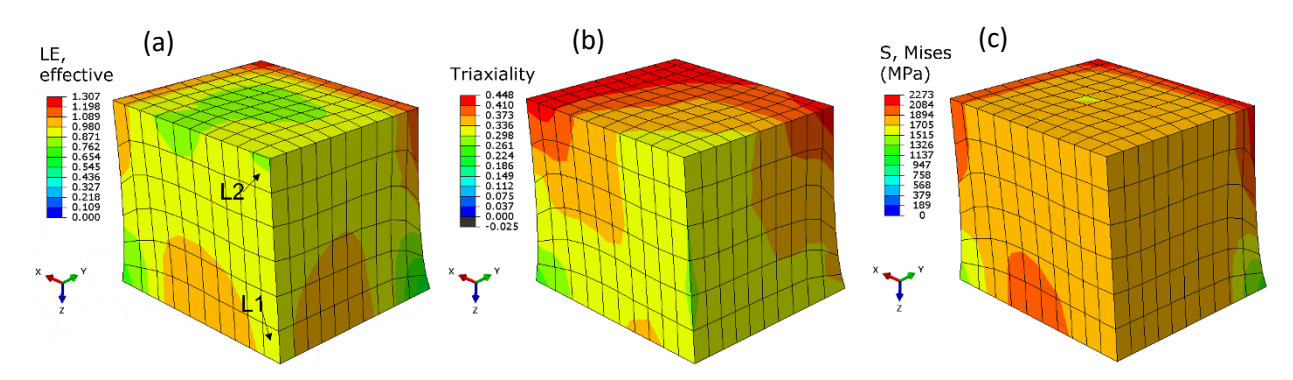


Figure 17: Contours of (a) effective strain, (b) triaxiality, and (c) von Mises stress at the end of notched tension simulation using the FE-EPSC with DMPT law.

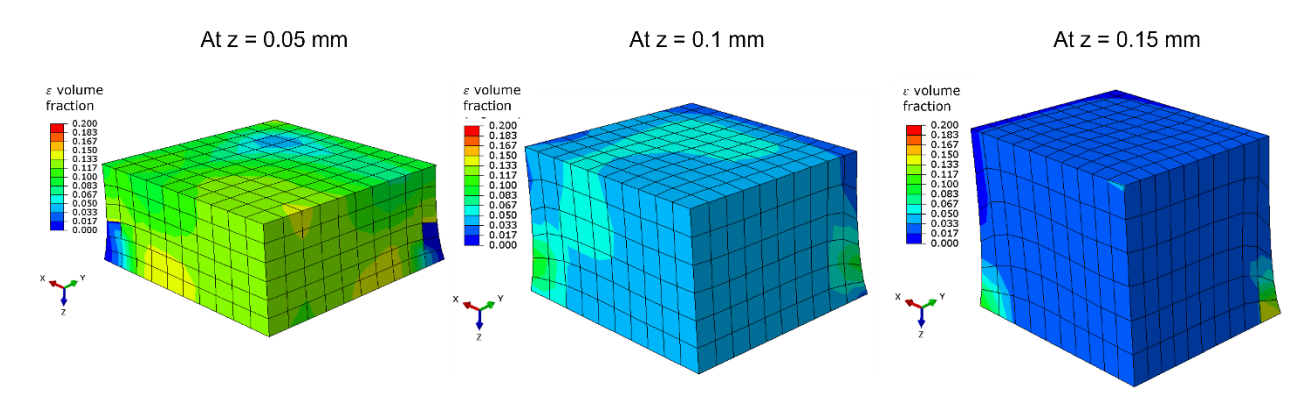


Figure 18: Spatial fields of  $\varepsilon$ -martensite volume fraction over the mesh at three displacements predicted using the FE-EPSC with DMPT law for the notched tension simulation. An increase and then a decrease of the intermediate  $\varepsilon$  phase is predicted as  $\varepsilon$  transforms to  $\alpha'$ -martensite.

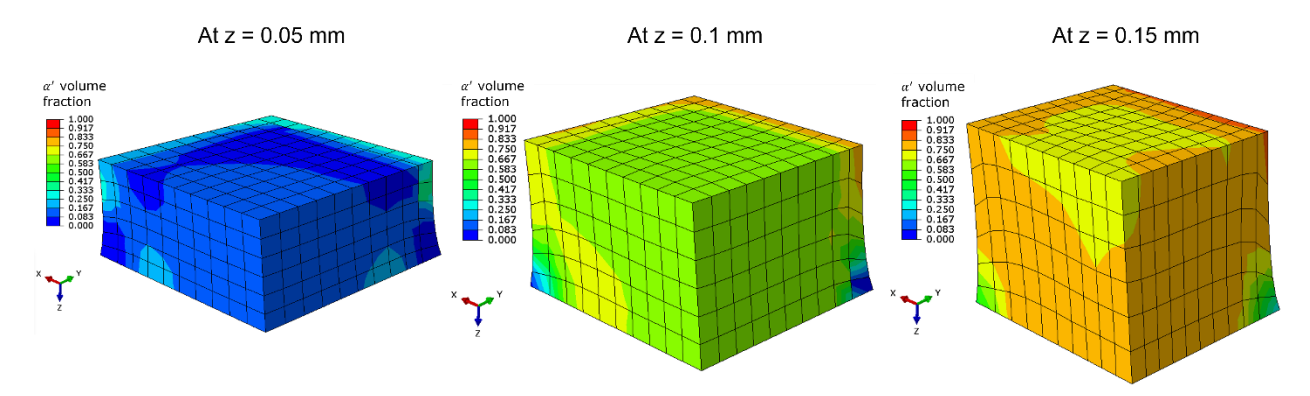


Figure 19: Spatial fields showing the evolution of  $\alpha'$ -martensite volume fraction over the mesh at three displacements predicted using the FE-EPSC with DMPT law for the notched tension simulation.

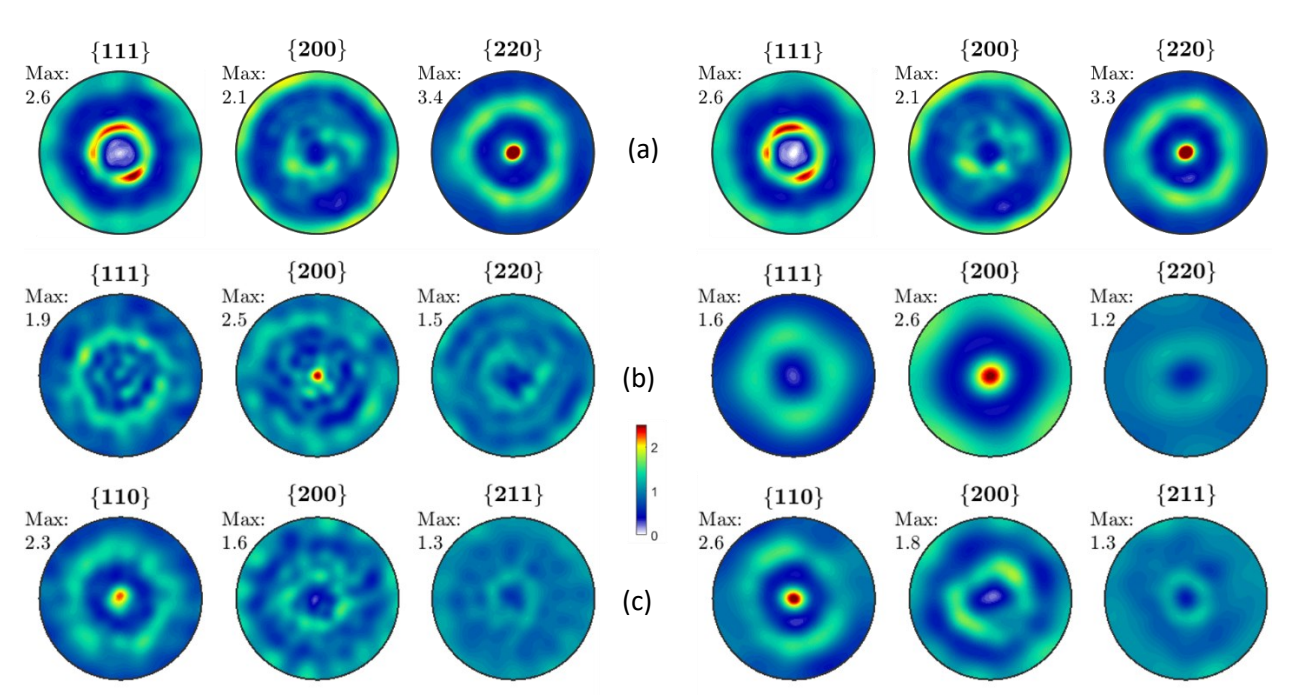


Figure 20: Pole figures showing measured and predicted texture evolution for the notched tension specimen: (a) initial FCC, (b) final FCC, and (c) final BCC textures. Measured pole figures on the left and simulated textures on the right. Simulated textures are extracted from location L2 on the model.

## 6. Summary and conclusions

In this work, we extended the martensite transformation laws from earlier works to incorporate strain-rate and temperature dependence into the initial slip resistance and phase transformation kinetic expressions, enabling the modeling of dynamic deformation conditions. The laws are incorporated into an implicit version of EPSC that operates as an implicit UMAT subroutine in Abaqus. The overall FE-EPSC implementation predicts macroscopic deformation based on the

deformation of constituent grains as a combination of anisotropic elasticity, crystallographic slip, and phase transformation, while the hardening is based on the evolution of dislocation density and explicit changes in the phase fractions. The laws are calibrated using wrought and additively manufactured SS304L data and then applied them to predict the geometry, volume fraction of phases, texture, and strength of additively manufactured SS304L samples subjected to impact and quasi-static notched tension deformation conditions. While the impact case of one AM 304L sample provided a broad range of strain level, strain-rate, and temperature conditions to evaluate predictive characteristics of the models, the quasi-static tension of a notched specimen of another AM 304L sample had varying strain levels, stress state, and triaxiality. Geometrical features and microstructures in terms of spatial fields of phase fraction and texture evolution were measured and used to experimentally verify the models. The main conclusions are:

- The calibrated and validated models can capture the strain path, strain-rate, temperature, and initial microstructure and texture sensitivity of martensitic transformation and the resulting deformation of stainless steels. Significantly, the models predict geometry, strength, phase fractions, and texture evolution while accounting for competing effects of strain level increasing the rate of transformation, and strain-rate and temperature decreasing the rate of transformation.
- While both OCPT and DMPT laws steam from a similar crystallographic formulation driven by the local stress state, the DMPT model can predict the intermediate  $\varepsilon$ -martensite phase and provide insights such as that  $\gamma \to \varepsilon$  transformation during tension is more rapid and substantial than during compression for the studied steels. Furthermore, the law reveals that the fraction of austenite grains that form  $\varepsilon$ -martensite phase during tension transforms more rapidly into  $\alpha$ '-martensite than those during compression.
- While both OCPT and DMPT laws predict well the general trend in the  $\alpha'$ -martensite volume fractions evolution, the  $\alpha'$ -martensite volume fractions predicted by the OCPT law are slightly higher than those predicted with the DMPT law. Nevertheless, the OCPT law predicts a slightly softer material than the DMPT law because the DMPT law evolves the intermediate  $\varepsilon$ -martensite phase that due to its hexagonal structure and underlying deformation mechanisms hardens the material.

# Acknowledgments

This research was sponsored by the U.S. National Science Foundation and was accomplished under the Grant No. OIA-1757371. Measurements presented here were performed at the Cornell High Energy Synchrotron Source which was supported by the National Science Foundation under NSF award DMR-1332208 at time of measurement. Los Alamos National Laboratory (LANL) is operated by Triad National Security, LLC, for the National Nuclear Security Administration of the U.S Department of Energy (Contract No. 89233218CNA000001). ZF, RP, EZA, BC, RM, and GTG-III acknowledge funding from Dynamic Materials Properties Campaign under DOE-NNSA.

# Appendix A

This appendix presents additional figures to provide more context of the experiment. Fig. A1 shows the notched tension specimen and the *in-situ* testing setup. Fig. A2 shows representative diffraction patterns at displacements of 0 mm and ~0.27 mm. Only austenite is present in the initial pattern, while both austenite and martensite phases are present at the higher displacement. Six austenite peaks and five martensite peaks are identified in the figure. At the large displacement, significant intergranular stress is present in the austenite as seen from the opposite shift in the 111 and 200 peaks (~2.1 and ~1.8 Å, respectively), which is also evidenced by the anti-symmetric and opposite swings in the difference curve for these peaks.

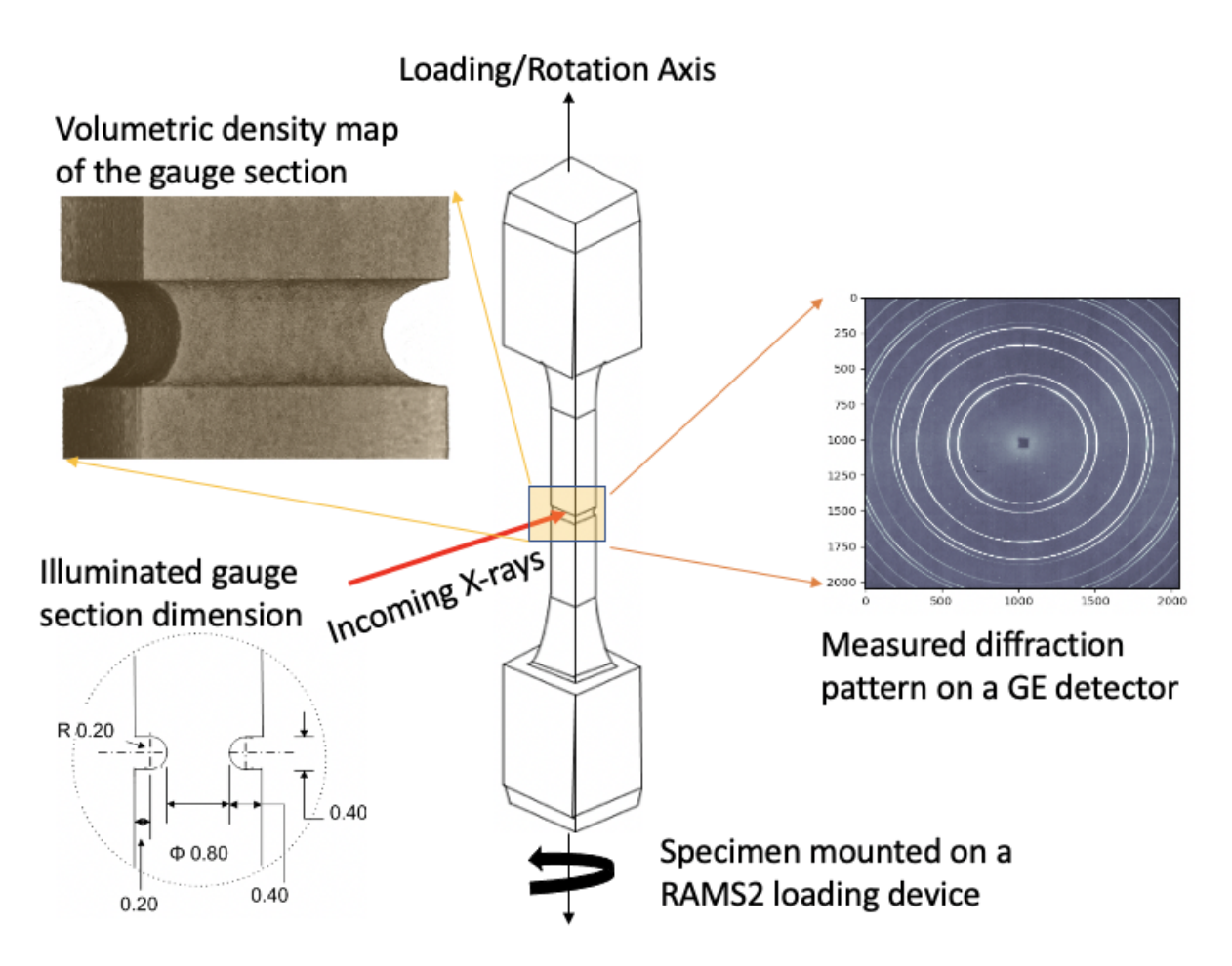


Figure A1: Schematic of the notched tensile specimen geometry and beam geometry for *in-situ* diffraction measurements performed at F2 beamline at CHESS. The sample was mounted on a RAMS 2 device (not shown in the figure) with its rotation axis parallel to the loading axis. The incoming X-ray beam illuminates the gauge section of the tensile specimen and diffraction and imaging data were recorded at different sample states, as the sample underwent tensile deformation. The dimensions are in mm.

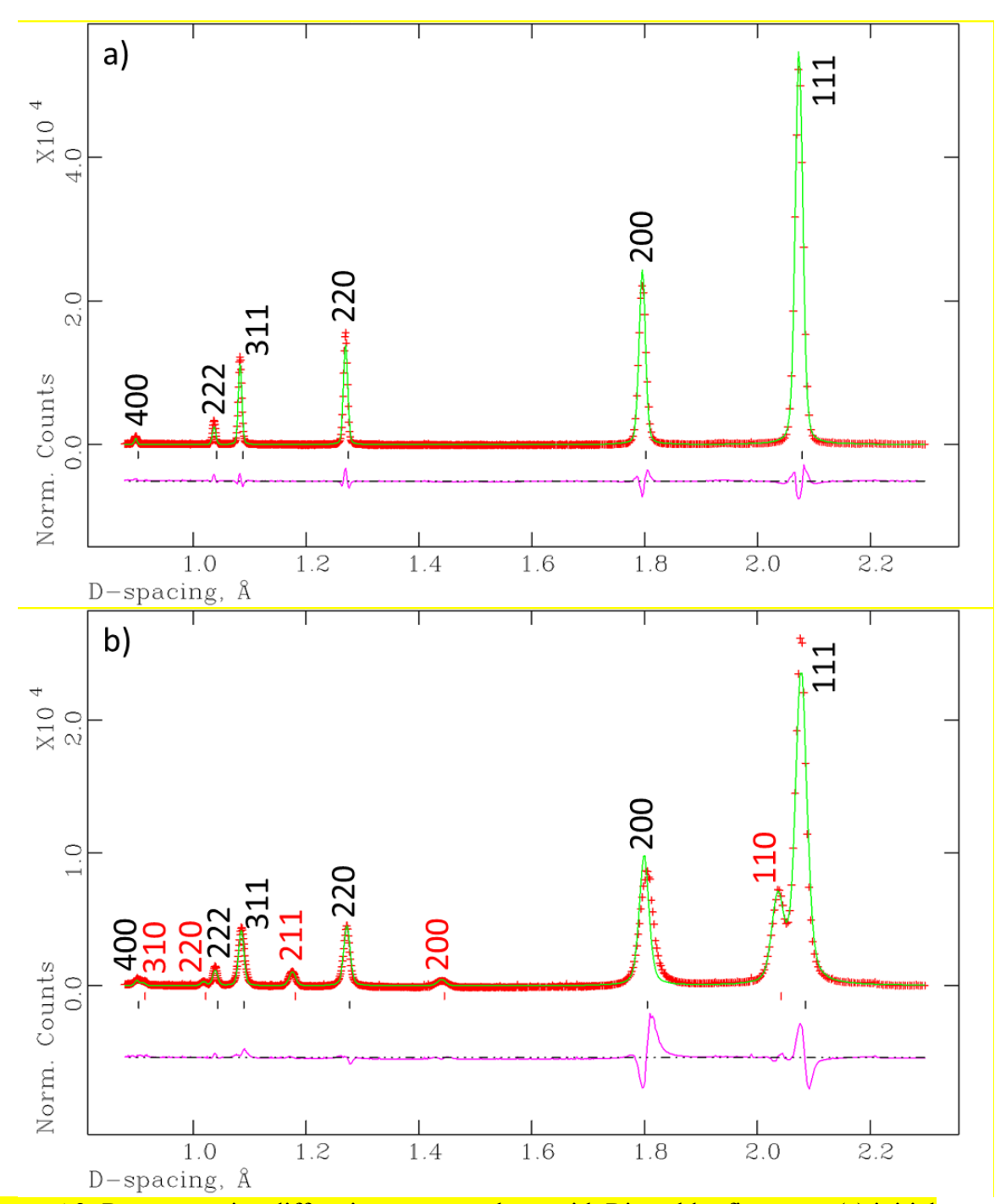


Figure A2: Representative diffraction patterns along with Rietveld refinement: (a) initial specimen containing only austenite and (b) the same specimen at a displacement of ~0.27 mm containing both austenite and martensite. Red symbols are measured data, green lines are the Rietveld fit, and the magenta lines are the difference curves. Black are hkls for austenite, while red hkls are for martensite.

#### References

- Ahmedabadi, P.M., Kain, V., Agrawal, A., 2016. Modelling kinetics of strain-induced martensite transformation during plastic deformation of austenitic stainless steel. Mater. Des. 109, 466-475.
- Angel, T., 1954. Formation of martensite in austenitic stainless steels. J. Iron Steel Inst. 177, 165-174.
- Ardeljan, M., Beyerlein, I.J., Knezevic, M., 2014. A dislocation density based crystal plasticity finite element model: Application to a two-phase polycrystalline HCP/BCC composites. J. Mech. Phys. Solids 66, 16-31.
- Ardeljan, M., Beyerlein, I.J., McWilliams, B.A., Knezevic, M., 2016a. Strain rate and temperature sensitive multi-level crystal plasticity model for large plastic deformation behavior: Application to AZ31 magnesium alloy. Int. J. Plast. 83, 90-109.
- Ardeljan, M., Knezevic, M., 2018. Explicit modeling of double twinning in AZ31 using crystal plasticity finite elements for predicting the mechanical fields for twin variant selection and fracture analyses. Acta. Mater. 157, 339-354.
- Ardeljan, M., Knezevic, M., Nizolek, T., Beyerlein, I.J., Mara, N.A., Pollock, T.M., 2015. A study of microstructure-driven strain localizations in two-phase polycrystalline HCP/BCC composites using a multi-scale model. Int. J. Plast. 74, 35-57.
- Ardeljan, M., Savage, D.J., Kumar, A., Beyerlein, I.J., Knezevic, M., 2016b. The plasticity of highly oriented nano-layered Zr/Nb composites. Acta. Mater. 115, 189-203.
- Barrett, T.J., Eghtesad, A., McCabe, R.J., Clausen, B., Brown, D.W., Vogel, S.C., Knezevic, M., 2019. A generalized spherical harmonics-based procedure for the interpolation of partial datasets of orientation distributions to enable crystal mechanics-based simulations. Materialia 6, 100328.
- Barrett, T.J., Knezevic, M., 2019. Deep drawing simulations using the finite element method embedding a multi-level crystal plasticity constitutive law: Experimental verification and sensitivity analysis. Computer Methods in Applied Mechanics and Engineering 354, 245-270.
- Barrett, T.J., McCabe, R.J., Brown, D.W., Clausen, B., Vogel, S.C., Knezevic, M., 2020. Predicting deformation behavior of α-uranium during tension, compression, load reversal, rolling, and sheet forming using elasto-plastic, multi-level crystal plasticity coupled with finite elements. J. Mech. Phys. Solids 138, 103924.
- Bathe, K.-J., 1996. Finite element procedures. Englewood Cliffs, N.J.: Prentice Hall.
- Beese, A.M., Mohr, D., 2011. Effect of stress triaxiality and Lode angle on the kinetics of strain-induced austenite-to-martensite transformation. Acta Materialia 59, 2589-2600.
- Beyerlein, I.J., Tomé, C.N., 2008. A dislocation-based constitutive law for pure Zr including temperature effects. Int. J. Plast. 24, 867-895.
- Bhadeshia, H.K.D.H., 2001. Worked examples in the Geometry of Crystals. The Institute of Metals North American Publications Center.
- Bhowmik, S., McWilliams, B.A., Knezevic, M., 2022a. Effect of powder reuse on tensile, compressive, and creep strength of Inconel 718 fabricated via laser powder bed fusion. Mater. Charact. 190, 112023.
- Bhowmik, S., Zhang, J., Vogel, S.C., Nene, S.S., Mishra, R.S., McWilliams, B.A., Knezevic, M., 2022b. Effects of plasticity-induced martensitic transformation and grain refinement on the evolution of microstructure and mechanical properties of a metastable high entropy alloy. J. Alloys Compd. 891, 161871.

- Bogers, A.J., Burgers, W.G., 1964. Partial dislocations on the {110} planes in the B.C.C. lattice and the transition of the F.C.C. into the B.C.C. lattice. Acta Metallurgica 12, 255-261.
- Bourke, M.A.M., Dunand, D.C., Ustundag, E., 2002. SMARTS a spectrometer for strain measurement in engineering materials. Applied Physics A 74, s1707-s1709.
- Bracke, L., Kestens, L., Penning, J., 2007. Transformation mechanism of α'-martensite in an austenitic Fe–Mn–C–N alloy. Scripta Materialia 57, 385-388.
- Bronkhorst, C.A., Mayeur, J.R., Livescu, V., Pokharel, R., Brown, D.W., Gray, G.T., 2019. Structural representation of additively manufactured 316L austenitic stainless steel. Int. J. Plast. 118, 70-86.
- Burgers, W.G., Klostermann, J.A., 1965. Influence of the direction of deformation on the transition of austenite into martensite. Acta Metallurgica 13, 568-572.
- Cahn, R.W., Haasen, P., Haasen, P., 1996. Physical Metallurgy, 4 ed. Elsevier Science.
- Christian, J.W., Mahajan, S., 1995. Deformation twinning. Prog. Mater. Sci. 39, 1-157.
- Daroju, S., Kuwabara, T., Knezevic, M., 2022a. Experimental characterization and crystal plasticity modeling of dual-phase steels subjected to strain path reversals. Mechanics of Materials 168, 104293.
- Daroju, S., Kuwabara, T., Sharma, R., Fullwood, D.T., Miles, M.P., Knezevic, M., 2022b. Experimental characterization and crystal plasticity modeling for predicting load reversals in AA6016-T4 and AA7021-T79. Int. J. Plast. 153, 103292.
- Das, Y.B., Forsey, A.N., Simm, T.H., Perkins, K.M., Fitzpatrick, M.E., Gungor, S., Moat, R.J., 2016. In situ observation of strain and phase transformation in plastically deformed 301 austenitic stainless steel. Materials & Design 112, 107-116.
- DebRoy, T., Wei, H., Zuback, J., Mukherjee, T., Elmer, J., Milewski, J., Beese, A.M., Wilson-Heid, A., De, A., Zhang, W., 2018. Additive manufacturing of metallic components–process, structure and properties. Progress in Materials Science 92, 112-224.
- Eghtesad, A., Barrett, T.J., Germaschewski, K., Lebensohn, R.A., McCabe, R.J., Knezevic, M., 2018a. OpenMP and MPI implementations of an elasto-viscoplastic fast Fourier transform-based micromechanical solver for fast crystal plasticity modeling. Advances in Engineering Software 126, 46-60.
- Eghtesad, A., Barrett, T.J., Knezevic, M., 2018b. Compact reconstruction of orientation distributions using generalized spherical harmonics to advance large-scale crystal plasticity modeling: Verification using cubic, hexagonal, and orthorhombic polycrystals. Acta. Mater. 155, 418-432.
- Eghtesad, A., Germaschewski, K., Knezevic, M., 2022. Coupling of a multi-GPU accelerated elasto-visco-plastic fast Fourier transform constitutive model with the implicit finite element method. Comput. Mater. Sci. 208, 111348.
- Eshelby, J.D., 1957. The determination of the elastic field of an ellipsoidal inclusion, and related problems. Proc R. Soc. Lond. A 241, 376-396.
- Feather, W.G., Ghorbanpour, S., Savage, D.J., Ardeljan, M., Jahedi, M., McWilliams, B.A., Gupta, N., Xiang, C., Vogel, S.C., Knezevic, M., 2019. Mechanical response, twinning, and texture evolution of WE43 magnesium-rare earth alloy as a function of strain rate: Experiments and multi-level crystal plasticity modeling. Int. J. Plast. 120, 180-204.
- Feather, W.G., Savage, D.J., Knezevic, M., 2021. A crystal plasticity finite element model embedding strain-rate sensitivities inherent to deformation mechanisms: Application to alloy AZ31. Int. J. Plast. 143, 103031.

- Fellinger, M.R., Hector Jr, L.G., Trinkle, D.R., 2019. Impact of solutes on the lattice parameters and elastic stiffness coefficients of hcp Fe from first-principles calculations. Comput. Mater. Sci. 164, 116-126.
- Feng, Z., Zecevic, M., Knezevic, M., 2021. Stress-assisted  $(\gamma \rightarrow \alpha')$  and strain-induced  $(\gamma \rightarrow \epsilon \rightarrow \alpha')$  phase transformation kinetics laws implemented in a crystal plasticity model for predicting strain path sensitive deformation of austenitic steels. Int. J. Plast. 136, 102807.
- Feng, Z., Zecevic, M., Knezevic, M., Lebensohn, R.A., 2022. Predicting extreme anisotropy and shape variations in impact testing of tantalum single crystals. International Journal of Solids and Structures 241, 111466.
- Ferreri, N.C., Feng, Z., Savage, D.J., Brown, D.W., Clausen, B., Sisneros, T.A., Knezevic, M., 2022. In-situ high-energy X-ray diffraction and crystal plasticity modeling to predict the evolution of texture, twinning, lattice strains and strength during loading and reloading of beryllium. Int. J. Plast. 150, 103217.
- Ferreri, N.C., Ghorbanpour, S., Bhowmik, S., Lussier, R., Bicknell, J., Patterson, B.M., Knezevic, M., 2019. Effects of build orientation and heat treatment on the evolution of microstructure and mechanical properties of alloy Mar-M-509 fabricated via laser powder bed fusion. Int. J. Plast. 121, 116-133.
- Ferreri, N.C., Pokharel, R., Livescu, V., Brown, D.W., Knezevic, M., Park, J.-S., Torrez, M.A., Gray, G.T., 2020a. Effects of heat treatment and build orientation on the evolution of  $\epsilon$  and  $\alpha'$  martensite and strength during compressive loading of additively manufactured 304L stainless steel. Acta. Mater. 195, 59-70.
- Ferreri, N.C., Vogel, S.C., Knezevic, M., 2020b. Determining volume fractions of  $\gamma$ ,  $\gamma'$ ,  $\gamma''$ ,  $\delta$ , and MC-carbide phases in Inconel 718 as a function of its processing history using an advanced neutron diffraction procedure. Mater. Sci. Eng. A 781, 139228.
- Franciosi, P., Zaoui, A., 1982. Multislip in f.c.c. crystals a theoretical approach compared with experimental data. Acta Metallurgica 30, 1627-1637.
- Frazier, W.E., 2014. Metal Additive Manufacturing: A Review. Journal of Materials Engineering and Performance 23, 1917-1928.
- Ghorbanpour, S., Alam, M.E., Ferreri, N.C., Kumar, A., McWilliams, B.A., Vogel, S.C., Bicknell, J., Beyerlein, I.J., Knezevic, M., 2020. Experimental characterization and crystal plasticity modeling of anisotropy, tension-compression asymmetry, and texture evolution of additively manufactured Inconel 718 at room and elevated temperatures. Int. J. Plast. 125, 63-79
- Ghorbanpour, S., Zecevic, M., Kumar, A., Jahedi, M., Bicknell, J., Jorgensen, L., Beyerlein, I.J., Knezevic, M., 2017. A crystal plasticity model incorporating the effects of precipitates in superalloys: Application to tensile, compressive, and cyclic deformation of Inconel 718. Int. J. Plast. 99, 162-185.
- Goetz, R.L., Semiatin, S.L., 2001. The adiabatic correction factor for deformation heating during the uniaxial compression test. Journal of Materials Engineering and Performance 10, 710-717.
- Goodchild, D., Roberts, W.T., Wilson, D.V., 1970. Plastic deformation and phase transformation in textured austenitic stainless steel. Acta Metallurgica 18, 1137-1145.
- Gray, G.T., Livescu, V., Rigg, P.A., Trujillo, C.P., Cady, C.M., Chen, S.-R., Carpenter, J.S., Lienert, T.J., Fensin, S.J., Knapp, C.M., Beal, R.A., Morrow, B., Dippo, O.F., Jones, D.R., Martinez, D.T., Valdez, J.A., 2016. L2 Milestone 5433: Characterization of Dynamic

- Behavior of AM and Conventionally Processed Stainless Steel (316L and 304L), United States.
- Gray, G.T., Livescu, V., Rigg, P.A., Trujillo, C.P., Cady, C.M., Chen, S.R., Carpenter, J.S., Lienert, T.J., Fensin, S.J., 2017. Structure/property (constitutive and spallation response) of additively manufactured 316L stainless steel. Acta Materialia 138, 140-149.
- Haidemenopoulos, G.N., Aravas, N., Bellas, I., 2014. Kinetics of strain-induced transformation of dispersed austenite in low-alloy TRIP steels. Materials Science and Engineering: A 615, 416-423.
- Herzog, D., Seyda, V., Wycisk, E., Emmelmann, C., 2016. Additive manufacturing of metals. Acta Materialia 117, 371-392.
- Hosford, W.F., Caddell, R.M., 1993. Metal forming mechanics and metallurgy. Prentice-Hall, Inc.
- Jun, J.-H., Choi, C.-S., 1998. Variation of stacking fault energy with austenite grain size and its effect on the MS temperature of  $\gamma \rightarrow \epsilon$  martensitic transformation in Fe–Mn alloy. Mater. Sci. Eng. A 257, 353-356.
- Khadyko, M., Dumoulin, S., Cailletaud, G., Hopperstad, O.S., 2016. Latent hardening and plastic anisotropy evolution in AA6060 aluminium alloy. Int. J. Plast. 76, 51-74.
- Kim, H., Lee, J., Barlat, F., Kim, D., Lee, M.-G., 2015. Experiment and modeling to investigate the effect of stress state, strain and temperature on martensitic phase transformation in TRIP-assisted steel. Acta Materialia 97, 435-444.
- Knezevic, M., Capolungo, L., Tomé, C.N., Lebensohn, R.A., Alexander, D.J., Mihaila, B., McCabe, R.J., 2012. Anisotropic stress-strain response and microstructure evolution of textured α-uranium. Acta. Mater. 60, 702-715.
- Knezevic, M., Carpenter, J.S., Lovato, M.L., McCabe, R.J., 2014a. Deformation behavior of the cobalt-based superalloy Haynes 25: Experimental characterization and crystal plasticity modeling. Acta. Mater. 63, 162-168.
- Knezevic, M., Crapps, J., Beyerlein, I.J., Coughlin, D.R., Clarke, K.D., McCabe, R.J., 2016. Anisotropic modeling of structural components using embedded crystal plasticity constructive laws within finite elements. International Journal of Mechanical Sciences 105, 227-238.
- Knezevic, M., Ghorbanpour, S., Ferreri, N.C., Riyad, I.A., Kudzal, A.D., Paramore, J.D., Vogel, S.C., McWilliams, B.A., 2021. Thermo-hydrogen refinement of microstructure to improve mechanical properties of Ti–6Al–4V fabricated via laser powder bed fusion. Mater. Sci. Eng. A 809, 140980.
- Knezevic, M., Landry, N.W., 2015. Procedures for reducing large datasets of crystal orientations using generalized spherical harmonics. Mechanics of Materials 88, 73-86.
- Knezevic, M., McCabe, R.J., Lebensohn, R.A., Tomé, C.N., Liu, C., Lovato, M.L., Mihaila, B., 2013. Integration of self-consistent polycrystal plasticity with dislocation density based hardening laws within an implicit finite element framework: Application to low-symmetry metals. J. Mech. Phys. Solids 61, 2034-2046.
- Knezevic, M., Nizolek, T., Ardeljan, M., Beyerlein, I.J., Mara, N.A., Pollock, T.M., 2014b. Texture evolution in two-phase Zr/Nb lamellar composites during accumulative roll bonding. Int. J. Plast. 57, 16-28.
- Knezevic, M., Zecevic, M., Beyerlein, I.J., Bingert, J.F., McCabe, R.J., 2015. Strain rate and temperature effects on the selection of primary and secondary slip and twinning systems in HCP Zr. Acta. Mater. 88, 55-73.

- Knockaert, R., Chastel, Y., Massoni, E., 2000. Rate-independent crystalline and polycrystalline plasticity, application to FCC materials. International Journal of Plasticity 16, 179-198.
- Kocks, U.F., Tomé, C.N., Wenk, H.-R., 1998. Texture and Anisotropy. Cambridge University Press, Cambridge, UK.
- Lagneborgj, R., 1964. The martensite transformation in 18% Cr-8% Ni steels. Acta Metall. 12, 823-843.
- Larson, A., Von Dreele, R., 1994. Los Alamos National Laboratory Report LAUR 86. Los Alamos National Laboratory, Los Alamos, NM.
- Laubscher, R.F., 2012. An evaluation of strain rate sensitivity of certain stainless steels. University of Johannesburg (South Africa).
- Lebedev, A.A., Kosarchuk, V.V., 2000. Influence of phase transformations on the mechanical properties of austenitic stainless steels. International Journal of Plasticity 16, 749-767.
- Lichtenfeld, J.A., Van Tyne, C.J., Mataya, M.C., 2006. Effect of strain rate on stress-strain behavior of alloy 309 and 304L austenitic stainless steel. Metallurgical and Materials Transactions A 37, 147-161.
- Lipinski, P., Berveiller, M., 1989. Elastoplasticity of micro-inhomogeneous metals at large strains. Int. J. Plast. 5, 149-172.
- Ludwigson, D., Berger, J.A., 1969. Plastic behaviour of metastable austenitic stainless steels. J Iron Steel Inst 207, 63-69.
- Mansourinejad, M., Ketabchi, M., 2017. Modification of Olson–Cohen model for predicting stress-state dependency of martensitic transformation. Materials Science and Technology 33, 1948-1954.
- Marki, R.E., Brindley, K.A., McCabe, R.J., Knezevic, M., 2022. Crystal mechanics-based thermo-elastic constitutive modeling of orthorhombic uranium using generalized spherical harmonics and first-order bounding theories. Journal of Nuclear Materials 560, 153472.
- Matsumura, O., Sakuma, Y., Takechi, H., 1987. Trip and its kinetic aspects in austempered 0.4C-1.5Si-0.8Mn steel. Scripta Metallurgica 21, 1301-1306.
- Maudlin, P., Gray, G., Cady, C., Kaschner, G., 1999. High—rate material modelling and validation using the Taylor cylinder impact test. Philosophical Transactions of the Royal Society of London A: Mathematical, Physical and Engineering Sciences 357, 1707-1729.
- Maudlin, P.J., Bingert, J.F., Gray Iii, G.T., 2003. Low-symmetry plastic deformation in BCC tantalum: experimental observations, modeling and simulations. Int. J. Plast. 19, 483-515.
- Murr, L.E., Staudhammer, K.P., Hecker, S.S., 1982. Effects of Strain State and Strain Rate on Deformation-Induced Transformation in 304 Stainless Steel: Part II. Microstructural Study. MTA 13, 627-635.
- Nagtegaal, J.C., Veldpaus, F.E., 1984. On the implementation of finite strain plasticity equations in a numerical model. Numerical methods in industrial forming processes, 351-371.
- Neil, C.J., Wollmershauser, J.A., Clausen, B., Tomé, C.N., Agnew, S.R., 2010. Modeling lattice strain evolution at finite strains and experimental verification for copper and stainless steel using in situ neutron diffraction. Int. J. Plast. 26, 1772-1791.
- Nugmanov, D., Knezevic, M., Zecevic, M., Sitdikov, O., Markushev, M., Beyerlein, I.J., 2018. Origin of plastic anisotropy in (ultra)-fine-grained Mg–Zn–Zr alloy processed by isothermal multi-step forging and rolling: Experiments and modeling. Mater. Sci. Eng. A 713, 81-93.
- Olson, G.B., Cohen, M., 1972. A mechanism for the strain-induced nucleation of martensitic transformations. Journal of the Less Common Metals 28, 107-118.
- Olson, G.B., Cohen, M., 1975. Kinetics of strain-induced martensitic nucleation. MTA 6, 791.

- Olson, G.B., Cohen, M., 1976. A general mechanism of martensitic nucleation: Part I. General concepts and the FCC → HCP transformation. Metallurgical Transactions A 7, 1897-1904.
- Petit, B., Gey, N., Cherkaoui, M., Bolle, B., Humbert, M., 2007. Deformation behavior and microstructure/texture evolution of an annealed 304 AISI stainless steel sheet. Experimental and micromechanical modeling. International Journal of Plasticity 23, 323-341.
- Pokharel, R., Balogh, L., Brown, D.W., Clausen, B., Gray, G.T., Livescu, V., Vogel, S.C., Takajo, S., 2018. Signatures of the unique microstructure of additively manufactured steel observed via diffraction. Scr. Mater. 155, 16-20.
- Polatidis, E., Morgano, M., Malamud, F., Bacak, M., Panzner, T., Van Swygenhoven, H., Strobl, M., 2020. Neutron Diffraction and Diffraction Contrast Imaging for Mapping the TRIP Effect under Load Path Change. Materials 13, 1450.
- Pronk, S., Frenkel, D., 2003. Large difference in the elastic properties of fcc and hcp hard-sphere crystals. Physical review letters 90, 255501.
- Ribárik, G., Gubicza, J., Ungár, T., 2004. Correlation between strength and microstructure of ball-milled Al–Mg alloys determined by X-ray diffraction. Materials Science and Engineering: A 387-389, 343-347.
- Risse, M., Lentz, M., Fahrenson, C., Reimers, W., Knezevic, M., Beyerlein, I.J., 2017. Elevated Temperature Effects on the Plastic Anisotropy of an Extruded Mg-4 Wt Pct Li Alloy: Experiments and Polycrystal Modeling. Metall. Mater. Trans. A 48, 446-458.
- Sames, W.J., List, F.A., Pannala, S., Dehoff, R.R., Babu, S.S., 2016. The metallurgy and processing science of metal additive manufacturing. International Materials Reviews 61, 315-360.
- Santacreu, P.-O., Glez, J.-C., Chinouilh, G., Fröhlich, T., 2006. Behaviour Model of Austenitic Stainless Steels for Automotive Structural Parts. steel research international 77, 686-691.
- Savage, D.J., Feng, Z., Knezevic, M., 2021. Identification of crystal plasticity model parameters by multi-objective optimization integrating microstructural evolution and mechanical data. Computer Methods in Applied Mechanics and Engineering 379, 113747.
- Schramm, R.E., Reed, R.P., 1975. Stacking fault energies of seven commercial austenitic stainless steels. MTA 6, 1345.
- Shade, P.A., Blank, B., Schuren, J.C., Turner, T.J., Kenesei, P., Goetze, K., Suter, R.M., Bernier, J.V., Li, S.F., Lind, J., Lienert, U., Almer, J., 2015. A rotational and axial motion system load frame insert for in situ high energy x-ray studies. Rev. Sci. Instrum. 86, 093902.
- Shin, H.C., Ha, T.K., Chang, Y.W., 2001. Kinetics of deformation induced martensitic transformation in a 304 stainless steel. Scr. Mater. 45, 823-829.
- Spencer, K., Véron, M., Yu-Zhang, K., Embury, J.D., 2009. The strain induced martensite transformation in austenitic stainless steels: Part 1 Influence of temperature and strain history. Materials Science and Technology 25, 7-17.
- Stringfellow, R.G., Parks, D.M., Olson, G.B., 1992. A constitutive model for transformation plasticity accompanying strain-induced martensitic transformations in metastable austenitic steels. Acta Metallurgica et Materialia 40, 1703-1716.
- Takajo, S., Brown, D.W., Clausen, B., Gray, G.T., Knapp, C.M., Martinez, D.T., Trujillo, C.P., Vogel, S.C., 2018. Spatially resolved texture and microstructure evolution of additively manufactured and gas gun deformed 304L stainless steel investigated by neutron diffraction and electron backscatter diffraction. Powder Diffraction 33, 141-146.
- Talonen, J., Hänninen, H., 2007. Formation of shear bands and strain-induced martensite during plastic deformation of metastable austenitic stainless steels. Acta. Mater. 55, 6108-6118.

- Turner, P.A., Tomé, C.N., 1994. A study of residual stresses in Zircaloy-2 with rod texture. Acta Metall. Mater. 42, 4143-4153.
- Vasilev, E., Zecevic, M., McCabe, R.J., Knezevic, M., 2020. Experimental verification of a crystal plasticity-based simulation framework for predicting microstructure and geometric shape changes: Application to bending and Taylor impact testing of Zr. International Journal of Impact Engineering 144, 103655.
- Wang, H., Jeong, Y., Clausen, B., Liu, Y., McCabe, R.J., Barlat, F., Tomé, C.N., 2016. Effect of martensitic phase transformation on the behavior of 304 austenitic stainless steel under tension. Materials Science and Engineering: A 649, 174-183.
- Wang, Z., Beese, A.M., 2019. Stress state-dependent mechanics of additively manufactured 304L stainless steel: Part 2 Characterization and modeling of macroscopic plasticity behavior. Materials Science and Engineering: A 743, 824-831.
- Wenk, H.-R., Cont, L., Xie, Y., Lutterotti, L., Ratschbacher, L., Richardson, J., 2001. Rietveld texture analysis of Dabie Shan eclogite from TOF neutron diffraction spectra. Journal of Applied Crystallography 34, 442-453.
- Yang, X.-S., Sun, S., Zhang, T.-Y., 2015. The mechanism of bcc  $\alpha'$  nucleation in single hcp  $\epsilon$  laths in the fcc  $\gamma \rightarrow$  hcp  $\epsilon \rightarrow$  bcc  $\alpha'$  martensitic phase transformation. Acta. Mater. 95, 264-273.
- Zecevic, M., Beyerlein, I.J., Knezevic, M., 2017. Coupling elasto-plastic self-consistent crystal plasticity and implicit finite elements: Applications to compression, cyclic tension-compression, and bending to large strains. Int. J. Plast. 93, 187-211.
- Zecevic, M., Beyerlein, I.J., McCabe, R.J., McWilliams, B.A., Knezevic, M., 2016a. Transitioning rate sensitivities across multiple length scales: Microstructure-property relationships in the Taylor cylinder impact test on zirconium. Int. J. Plast. 84, 138-159.
- Zecevic, M., Knezevic, M., 2017. Modeling of Sheet Metal Forming Based on Implicit Embedding of the Elasto-Plastic Self-Consistent Formulation in Shell Elements: Application to Cup Drawing of AA6022-T4. JOM 69, 922-929.
- Zecevic, M., Knezevic, M., 2018a. Latent hardening within the elasto-plastic self-consistent polycrystal homogenization to enable the prediction of anisotropy of AA6022-T4 sheets. Int. J. Plast. 105, 141-163.
- Zecevic, M., Knezevic, M., 2018b. A new visco-plastic self-consistent formulation implicit in dislocation-based hardening within implicit finite elements: Application to high strain rate and impact deformation of tantalum. Computer Methods in Applied Mechanics and Engineering 341, 888-916.
- Zecevic, M., Knezevic, M., 2019. An implicit formulation of the elasto-plastic self-consistent polycrystal plasticity model and its implementation in implicit finite elements. Mechanics of Materials 136, 103065.
- Zecevic, M., Knezevic, M., Beyerlein, I.J., McCabe, R.J., 2016b. Texture formation in orthorhombic alpha-uranium under simple compression and rolling to high strains. Journal of Nuclear Materials 473, 143-156.
- Zecevic, M., Knezevic, M., Beyerlein, I.J., Tomé, C.N., 2015. An elasto-plastic self-consistent model with hardening based on dislocation density, twinning and de-twinning: Application to strain path changes in HCP metals. Mater. Sci. Eng. A 638, 262-274.
- Zecevic, M., Knezevic, M., McWilliams, B., Lebensohn, R.A., 2020. Modeling of the thermomechanical response and texture evolution of WE43 Mg alloy in the dynamic

- recrystallization regime using a viscoplastic self-consistent formulation. Int. J. Plast. 130, 102705.
- Zecevic, M., Korkolis, Y.P., Kuwabara, T., Knezevic, M., 2016c. Dual-phase steel sheets under cyclic tension—compression to large strains: Experiments and crystal plasticity modeling. J. Mech. Phys. Solids 96, 65-87.
- Zecevic, M., Upadhyay, M.V., Polatidis, E., Panzner, T., Van Swygenhoven, H., Knezevic, M., 2019. A crystallographic extension to the Olson-Cohen model for predicting strain path dependence of martensitic transformation. Acta. Mater. 166, 386-401.
- Zhu, Z., Li, W., Nguyen, Q.B., An, X., Lu, W., Li, Z., Ng, F.L., Ling Nai, S.M., Wei, J., 2020. Enhanced strength–ductility synergy and transformation-induced plasticity of the selective laser melting fabricated 304L stainless steel. Additive Manufacturing 35, 101300.